

# Discrimination of thermodynamic and kinetic contributions to the heavy rare earth element patterns in metamorphic garnet

Matthias Konrad-Schmolke<sup>1</sup>, Ralf Halama<sup>2</sup>, David Chew<sup>3</sup>, Céline Heuzé<sup>1</sup>, Jan De Hoog<sup>4</sup> and Hana Ditterova<sup>5</sup>

<sup>1</sup>Department of Earth Sciences, University of Gothenburg, Sweden

<sup>2</sup>School of Geography, Geology and the Environment, Keele University, UK

<sup>3</sup>Department of Geology, School of Natural Sciences, Trinity College Dublin, Ireland

<sup>3</sup> School of GeoSciences, Grant Institute, James Hutton Road, Edinburgh, EH9 3FE, UK

<sup>5</sup>Earth Science Department, University of Potsdam, Germany

## Abstract

Variations of rare earth element (REE) concentrations in metamorphic garnet are an important source of information of geodynamic and geochemical processes in the deeper Earth. In order to extract this information, the thermodynamic equilibrium and kinetic contributions of the REE uptake in garnet must be distinguished and quantified. Utilizing high resolution trace element and  $\mu$ -Raman mapping together with combined thermodynamic-geochemical-diffusion models we demonstrate that the equilibrium and kinetic aspects of the REE uptake in metamorphic garnet can be discriminated by interpreting 2D trace element mapping in a single sample. The heavy (H) REE (Tb to Lu) zoning in the investigated garnet from a high-pressure blueschist comprises an inner part with an overall decrease from core to inner rim, followed by a concentric zone of HREE enrichment and a drastic HREE decrease towards the outermost rim. The central peak in the garnet core decreases in intensity with decreasing atomic number of the REE. The broad overall shape of this pattern resembles those often observed in metamorphic garnets from different rock types and tectonic settings. Superimposed on this trend is a concentric pattern of minor recurring fluctuations in the HREE concentrations with at least six regularly spaced sets of peaks and troughs along the entire garnet radius. Comparison of the observed inclusion suite, the trace element maps and thermodynamic-geochemical models show that the inner part with decreasing HREE concentrations results from fractional garnet growth in an unchanged mineral assemblage, whereas the REE enrichment zone is caused by the breakdown of titanite. We suggest that the width of the central peak is controlled by the bulk permeability of the interconnected transport

matrix and the fraction of matrix minerals that the garnet equilibrates with. The superimposed REE fluctuations result from changing element transport properties of the host rock and mark recurring changes from equilibrium REE uptake to transport-limited REE uptake in garnet. Such fluctuating element transport properties can be best explained by pulse-like fluid fluxes that rhythmically change the interconnectivity of the intercrystalline transport matrix. Increasing numbers of published spatially highly resolved REE analyses show that such trace element fluctuations are common in metamorphic garnet indicating that recurring changes in rock permeabilities due to pulsed fluid fluxes are a common phenomenon during metamorphism.

## **Introduction**

Garnet, one of the major phases in many metamorphic rocks, is by far the most versatile mineral with respect to the recording of geodynamic and geochemical processes (e.g., Spear and Selverstone 1983; Lasaga and Jiang 1995; Ganguly et al., 1996; O'Brien, 1997; Chernoff and Carlson 1997; Spear and Daniel 2001; Yang and Rivers 2001; Konrad-Schmolke et al., 2005; Inui 2006; Gaidies et al., 2006; Gaidies et al., 2015; George and Gaidies 2017). It is stable over a wide pressure and temperature range and thus can grow continuously from shallow depths to high pressures, thereby recording processes in the entire lithosphere. Its major and trace element composition is sensitive to subtle chemical changes in the surrounding rock volume (e.g., Jamtveit and Hervig 1994; Yang and Rivers 2002; Mc Cammon and Kapylova 2004; Moyen 2009; Kotkova and Harley 2010), which makes garnet an excellent recorder of mineral reactions, fluid-rock interaction and element transport processes in the host rock (e.g., Skora et al., 2006; Konrad-Schmolke et al., 2008b). Furthermore, due to the extremely slow diffusive intracrystalline element transport in garnet (e.g., Tirone et al., 2005; Carlson 2006, 2012), compositional and isotopic growth zonation is very commonly preserved and can be used to extract information about geological processes from single garnet crystals (e.g., Hermann and Rubatto 2003; Whitehouse and Platt 2003; Caddick et al., 2010) and provide information relevant for the analysis of mineral nucleation and growth kinetics (George and Gaidies 2017; George et al., 2018). This holds especially true for rare earth elements (REE) growth zonation, which is commonly preserved even if major element variations are diffusively modified (e.g., Kotkova and Harley 2010). As garnet is a major REE-bearing mineral and fractionates strongly between light (L) and heavy (H) REEs, REE concentrations, REE variations and REE distribution patterns extracted from garnet are often interpreted in



terms of reflecting geodynamic and geochemical processes in the host rock (e.g., Rubatto et al., 2020). However, it is still heavily debated and unclear to what extent REE uptake in garnet is controlled by thermodynamic and geochemical parameters, such as mineral reactions or changing fluid compositions in the host rock (e.g., Konrad-Schmolke et al., 2008), or whether kinetic aspects, such as sluggish element transport in the host rock (e.g., Skora et al., 2006), play the key role during REE uptake. It is evident that both factors, thermodynamic and kinetic, are crucial for the characterization and quantification of geodynamic processes. This is because mineral reactions recorded in the REE patterns reflect the reaction path of the rock, whereas element transport properties can be tied to rock permeabilities and fluid percolation. Furthermore, the distinction between thermodynamic and kinetic contributions to garnet growth is important for garnet geochronology as the distribution of Lu and Sm within the garnet influences the ages derived from Lu/Hf and Sm/Nd geochronology. Unambiguous evidence for the effects of both contributions recorded in a suitable sample is still lacking, predominantly due to the lack of sufficiently spatially resolved REE analyses in single garnet crystals.

We employ high-resolution trace element mapping, utilizing laser ablation inductively coupled plasma mass spectrometry (LA-ICP-MS), that illustrates subtle changes in the heavy rare earth element (HREE) composition of a single garnet from a subducted and exhumed high-pressure rock. When combined with  $\mu$ -Raman mapping that visualizes the distribution of  $\mu\text{m}$ -scale mineral inclusions in the garnet and compared to thermodynamic-geochemical models, we are able to distinguish between thermodynamic and kinetic contributions to the REE uptake in garnet. Thus, we obtain detailed information about the reaction history of the host rock as well as its element transport properties during garnet growth. Characteristic REE patterns together with systematic REE variations in our sample reflect the combined effects of mineral reactions as well as recurring fluctuations in rock permeabilities during high pressure metamorphism.

## **Geological framework**

The sample investigated in this work is a garnet-bearing blueschist from the high-pressure Punta Balandra unit in the Dominican Republic on the island of Hispaniola. In the north-western part of Hispaniola, on the Samana peninsula, various types of high-pressure basement rocks are exposed (see Fig. 1 in Escuder-Virueite and Pérez-Estaún 2006). Among these are blueschist, eclogites, serpentinites and *mélange* associations that are formed at different levels of a Late-Jurassic to Eocene subduction complex (Nagle

1974). The rocks of the Punta Balandra unit, located at the southern shore of the Samana peninsula, record the early stages of southwest-directed subduction of the North American plate beneath the Caribbean island arc (Mann et al., 1991). Within the Punta Balandra Unit mafic high-pressure boudins and blocks are intercalated with mica schists and carbonates.

During subduction the Punta Balandra unit recorded a prograde pressure-temperature ( $P$ - $T$ ) evolution along a steep  $P$ - $T$  gradient between about 0.5 GPa and 350°C and 2.4 GPa and 650°C (Escuder-Virueite and Pérez-Estaún 2006). Different stages of the subduction process are excellently preserved in various forms of mineral assemblages either as numerous inclusions in large garnet porphyroblasts in different rock types or as metastable matrix assemblages in rocks with different extents of pro- and retrograde metamorphic overprinting. Several detailed petrological and geochronological works that focussed on the rocks of the Punta Balandra unit enable these rocks to be employed as a natural laboratory for the investigation of subduction processes (Joyce 1991; Concalves et al., 2000; Catlos and Sorensen 2003; Escuder-Virueite et al., 2011a, b). Based on thermodynamic modelling and conventional thermobarometry, the metamorphic evolution of the Punta Balandra rocks can be reconstructed in detail and six distinct metamorphic stages have been distinguished based on different co-existing mineral assemblages by Escuder-Virueite and Pérez-Estaún (2006).

*Stage 1:* In some eclogite-facies garnet porphyroblasts, rare relics of the early prograde greenschist- to blueschist-facies stages are preserved in the form of inclusions of calcic-amphibole, albite, chlorite and phengite. The inferred pressure and temperature conditions are around 0.5 GPa and 450°C.

*Stage 2:* Lawsonite inclusions and their pseudomorphic replacement by epidote and white mica together with rutile, phengite, paragonite and clinopyroxene inclusions in garnet are interpreted as relics of the lawsonite-blueschist-facies stage. Pressure and temperature conditions during that stage were between 0.8 and 1.5 GPa at temperatures between 350 and 450°C.

*Stage 3:* Prograde blueschist- to eclogite facies mineral assemblages of garnet, epidote, phengite, paragonite, clinopyroxene and rutile are also found as inclusions in some eclogite-facies garnet porphyroblasts. This stage corresponds to pressure and temperature conditions around 1.5 to 1.8 GPa at 500 – 550°C.

*Stage 4:* Peak eclogite-facies metamorphism of the rocks is reflected in well-preserved garnet+clinopyroxene+phengite+rutile+quartz assemblages. Peak metamorphic conditions were in the order of 2.4 GPa and around 650°C.

*Stage 5:* The eclogites are partially hydrated and statically retrogressed to garnet-bearing blueschists with the matrix assemblage sodic amphibole + titanite + epidote + quartz + phengite within which cm-sized eclogite-facies garnet porphyroblasts can be found. This stage is related to fluid influx and metasomatism between peak metamorphic conditions and 1.3 GPa at 550°C along a cold retrograde exhumation path.

*Stage 6:* Late stage greenschist-facies retrogression is reflected in the breakdown of garnet to form epidote and chlorite as well as in the formation of albite and calcic amphibole from clinopyroxene and sodic amphibole, respectively. This last metamorphic imprint occurred at around 0.8 GPa and below 500°C.

## **Sample description**

The sampled rock is a garnet-bearing blueschist statically equilibrated during early *Stage five* of this subdivision. The blueschist is unfoliated with a medium-grained matrix consisting of up to several mm-large, often euhedral, sodic amphibole grains and quartz aggregates within which up to cm-sized euhedral garnet porphyroblasts are homogeneously distributed (Fig. 1a). Minor phases in the matrix are up to several mm in size and include titanites (often euhedral), chlorite that partly replaces garnet and amphibole, white mica, epidote, apatite, zircon and minor iron hydroxide grains that reflect very late weathering of chlorite and sodic amphibole. Sodic amphibole and garnet are inclusion-rich. In sodic amphibole the most abundant inclusion phase is titanite, most of which has rutile cores or at least small rutile inclusions. Less abundant inclusions are white mica, epidote and omphacite (Fig. 1b and c) that is likely relict from the peak metamorphic phase assemblage. Inclusion phases in the cores of the large garnet porphyroblasts are titanite (lacking rutile inclusions), apatite, epidote, minor zircon and quartz. In the garnet rims rutile is the most abundant inclusion phase, but epidote, apatite, zircon and white mica can also be found in the outermost parts of the grains. It is notable that apatite, epidote and zircon grains are abundant as inclusions throughout the entire porphyroblasts (see electronic supplementary material) and that almost all of the matrix titanites have rutile cores or inclusions.

Detailed petrological investigations of garnets in different rocks from the Punta Balandra unit demonstrated that garnet records a significant portion of the prograde  $P$ - $T$  path between 420°C and 575°C and 1.2 to 2.0 GPa and hence documents the physical and chemical history of high pressure/low temperature (HP/LT) metamorphic processes (Escuder-Virueite and Pérez-Estaún 2006). The sample in this work was chosen because of its large euhedral garnet grains that, judged from the major element compositional variations and from the inclusion assemblage, record large parts of the prograde history of the host rock, although the matrix mineral assemblage is reflecting a later, blueschist-facies stage of the rock's metamorphic evolution.

## **Methods**

### ***Analytical and computational procedures***

All major and trace element mineral compositions were measured in a polished thin section that was prepared at the Institute of Earth and Environmental Science at Potsdam University in Germany. In order to choose a garnet crystal that is cut closest to the centre, the largest idiomorphic garnet in the thin section with the highest spessartine component in the core was chosen for further investigations.

#### *Electron Probe Micro Analyses (EPMA)*

Major element mapping and spot analyses of the chosen garnet were carried out with a JEOL JXA-8200 electron probe micro-analyser at the Institute of Earth and Environmental Sciences at Potsdam University. Instrumental conditions during map measurements were set at 15 kV accelerating voltage, 200 nA beam current, 2 µm beam size and a dwell time of 200 ms. For the EPMA spot analyses the acceleration voltage was 15 kV with a beam current of 15 nA and a beam diameter of 2 µm. Detector counting times were 20s on peaks and 10s on background on both sides of the peaks.

#### *Laser ablation inductively coupled plasma mass spectrometry (LA ICP MS)*

The 2-dimensional element maps were carried out with the Teledyne Photon Machines Analyte Excite laser ablation system equipped with an aerosol rapid introduction system (ARIS) coupled to an Agilent 7900 Quadrupole Inductively-Coupled-Plasma Mass Spectrometer (iCapQs ICP-MS) at Trinity College Dublin, Ireland. The acquisition was performed by defining a selected rectangular area comprised of successive line scans (rasters) over the garnet crystal (*cf* Ubide et al., 2015). Each raster employed overlapping

12  $\mu\text{m}$  spot ablations with a  $100\text{ }\mu\text{m s}^{-1}$  scan velocity and a 51 Hz repetition rate. During the mapping session, 20 major and trace elements were acquired with the dwell time set at 100  $\mu\text{s}$ , while NIST610 standard glass (Jochum et al., 2011) measured at the start and end of every mapping sequence. In particular, Ca, Mn and REE+Y elemental maps were measured for garnet investigation and Sr, P and Ti maps to aid detection of mineral inclusions. The total analysis time was 7.5 h for a  $3.5\times 4.5\text{ mm}$  area of the garnet sample.

#### *Data reduction*

Time-resolved laser ablation ICP-MS Data were reduced by the Trace\_Elements data reduction scheme (DRS) in the Iolite v2.5 data reduction software (Paton et al., 2011), which runs under IGOR Pro 6.3 (WaveMetrics, Inc.). The selected DRS setting employed semi-quantitative normalization relative to the reference material NIST 610 glass. Primary trace element 2D maps were generated using the Iolite CellSpace Image function. Later data processing, such as profile extraction from the trace element mapping as well as detailed selections from the original maps were performed with MATLAB® version R2018b. MATLAB® scripts are available on request from the first author. It is important to mention that in order to avoid misinterpretation of the REE concentrations and REE distribution patterns in garnet by inclusion phases, such as titanite, apatite and epidote, we discarded all analyses from the mapping that contained more than 1000 ppm, 10 ppm and 1 ppm of Ti, P and Sr, respectively. Wherever full maps are shown for clarity this is indicated in the figure captions. Profiles that were extracted from the maps were low-pass frequency filtered to eliminate analytical scatter.

#### *Confocal $\mu$ -Raman spectroscopy*

Laser-induced Raman measurements and mapping were carried out at room temperature using a Horiba (Jobin Yvon) LabRam HR Evolution at Gothenburg University. The samples were excited with an air-cooled frequency doubled 532nm Nd-YAG laser utilizing an Olympus 50 $\times$  objective (numerical aperture = 0.9). The lateral resolution of the unpolarized confocal laser beam was in the order of  $1\mu\text{m}$ , the vertical extent of the acquisition volume was about  $3\mu\text{m}$ . For the Raman mappings the laser spot was focused several  $\mu\text{m}$  beneath the sample surface, whereas for detection of individual grains the entire depth of the thin section was scanned. Spot spectra were generated in the range of 100 to  $4000\text{ cm}^{-1}$  utilizing a 600 grooves/cm grating and a thermoelectric cooled electron multiplier CCD including a front illuminated  $1600\times 200$  pixel chip. The spectral resolution

on polished sample was in the order of  $1\text{ cm}^{-1}$ . The wavenumber calibration was done using the  $520.7\text{cm}^{-1}$  Raman band on a polished silicon wafer with a wavenumber accuracy usually better than  $0.5\text{ cm}^{-1}$ .

Raman mapping was performed with a spatial resolution of  $5\text{ }\mu\text{m}$  with a continuous laser beam and a motorized stage, the speed of which was adjusted to the integration time of the measurements. Data processing of the Raman mapping was performed with the Horiba LabRam® software version 6. All spectra are background and slope corrected and despiked automatically. The height of the respective peaks was used to produce the maps.

### *Secondary Ion Mass Spectrometry*

Concentrations of  $\text{H}_2\text{O}$  and fluid mobile element (FME), namely Li, B, F and Cl, as well as Mg, Ti, Y and Ce concentrations in garnet were measured in gold-coated thin sections utilizing a Cameca 7f-GEO secondary ion mass spectrometer with Hyperion RF plasma ion source at the Edinburgh Ion Microprobe Facility (EIMF). A focussed  $5.1\text{ nA }^{16}\text{O}^-$  primary beam with an impact energy of  $18.5\text{ keV}$  was used to sputter an area of ca.  $20\times 20\text{ }\mu\text{m}$  of the sample surface, generating secondary ions. Positive secondary ions with an energy of  $50\pm 20\text{ eV}$  were extracted into a double-focussing mass spectrometer. Energy filtering reduces matrix effects as well as certain molecular interferences. The various isotopes were analysed by peak switching of the magnet and ion signals were counted with an electron multiplier. Prior to analysis, the area to be analysed was precleaned for  $180\text{ s}$  by rastering the primary beam over an area of  $35\times 35\text{ }\mu\text{m}$ . This reduces particularly the  $^1\text{H}$  background considerably (see below for details). Secondary ion beam centring and mass calibration peak adjustment were undertaken prior to each analysis in an automated routine. During analysis, an effective field aperture of  $25\text{ }\mu\text{m}$  was used. The mass resolution used was  $600\text{ (M}/\Delta\text{M})$  to maximise ion transmission. Count times were  $2\text{ s}$  for  $^{26}\text{Mg}$ ,  $^{30}\text{Si}$  and  $^{47}\text{Ti}$ ,  $3\text{ s}$  for  $^1\text{H}$ ,  $^7\text{Li}$  and  $^{89}\text{Y}$ ,  $5\text{ s}$  for  $^{11}\text{B}$  and  $^{140}\text{Ce}$ , and  $10\text{ s}$  for  $^{19}\text{F}$  and  $^{35}\text{Cl}$  per cycle (magnet sweep), where each analysis consisted of six cycles.

Count rates were converted into concentrations by comparing Si-normalised count rates of samples with those of calibration standards with known  $\text{SiO}_2$  and trace element contents. The following standards were used: a set of five garnets from Reynes et al. (2018) for  $\text{H}_2\text{O}$  ( $\text{H}_2\text{O}$  range  $0\text{--}834\text{ }\mu\text{g/g}$ ); ALV519-4-1 MORB glass for F, MgO,  $\text{TiO}_2$ , Y and Ce (Jackson et al., 2015; Kumamoto et al., 2017); experimental basaltic glass St8.1.A9 from Lesne et al. (2011) for Cl; and the same glass standard employed for Li and B using

concentrations determined independently at EIMF. The measured  $^1\text{H}$  signal of the water-free garnet was used as a blank correction for  $\text{H}_2\text{O}$  calibration. Samples were kept in an airlock at high vacuum ( $2.5 \times 10^{-8}$  mbar), whereas measurements took place in a sample chamber at  $8.9 \times 10^{-10}$  mbar. Calibration slopes of  $\text{H}_2\text{O}$  for garnet and basaltic glass differed by only 11%, which is very close considering much larger fractionations observed for other nominally anhydrous minerals, such as clinopyroxene and orthopyroxene (e.g., Gleeson et al., 2022).

### *Thermodynamic-geochemical modelling*

The thermodynamic-geochemical modelling approach is based on an incremented Gibbs energy minimisation forward model of the phase assemblage along the sample's  $P$ - $T$  trajectory and a mass-balanced REE distribution among the stable phases at each increment (e.g., Konrad-Schmolke et al., 2008b; Konrad-Schmolke et al., 2011). Modal proportions and composition of stable phases were calculated at 200 increments along a high-pressure  $P$ - $T$  trajectory that starts at  $420^\circ\text{C}/1.2$  GPa and ends at  $570^\circ\text{C}/1.95$  GPa. It was chosen to reflect the pressure and temperature interval for garnet growth (Escuder-Virue and Pérez-Estaún 2006).

Phase relations and compositions along the  $P$ - $T$  trajectory were calculated assuming water fractionation and fractional garnet crystallisation in the chemical system Mn, Na, Ca, K, Fe, Mg; Al, Si, O, H (MnNCKFMASH) utilising Gibbs energy minimisation performed with the software package Theriak (de Capitani and Brown 1987), the data extraction procedure published in Lanari et al. (2014), and the Holland and Powell (1998) database with recent updates. Solid solution models employed are feldspar (Baldwin et al., 2005), garnet (Holland and Powell 1998), omphacite (Holland and Powell 1996), chlorite (Holland et al., 1998), white mica (Keller et al., 2005), biotite (White et al., 2007), talc (Holland and Powell 1998), amphibole (White et al., 2003) and epidote (ideal). A comparison of the results utilising a different set of thermodynamic standard state data and solid solution models is provided in the electronic supplementary material. Water as a thermodynamic phase was considered pure  $\text{H}_2\text{O}$  throughout all modelling. The chemical potential of oxygen was constrained by an ilmenite-magnetite-rutile (IMR) buffer (Konrad-Schmolke et al., 2008a). The chosen bulk rock composition used for the calculations is given in Table 1.

For the REE modelling we consider REEs as behaving thermodynamically passively, i.e. without influence on the major element composition and stability of the phases, and that the distribution of REEs among the stable phases can be described by bulk partition coefficients. We calculated the REE distribution among the modelled phases at every modelled  $P$ - $T$  increment using mass balance constraints and internally consistent partition coefficients (Table 2). Bulk distribution coefficients were calculated at each increment based on the thermodynamically modelled phase assemblage. REEs incorporated in garnet and water were fractionated from the system according to the modelled modal amounts of these phases. The initial trace element concentrations of every element in the bulk rock are given in Table 3 and a more detailed description of the algorithm can be found in the electronic supplementary material.

## Results

The euhedral garnet grain chosen for detailed analysis has a diameter of about 9 mm and clearly exhibits two different growth zones (Figs. 1a and 2a). A core region that is slightly darker than the rim comprises 65-70 % of the area of the section through the grain. The core contains numerous inclusions of very fine-grained titanite together with lower abundances of apatite (ap), zircon (zrc) and quartz (qtz). The lighter-coloured rim overgrowth has fewer inclusions, which consist of apatite, epidote, white mica and relatively large rutile (rt) grains that can be clearly seen as brown inclusion phases (Fig. 2a). The garnet rims show no or very limited signs of post-growth resorption.

### *Compositional zoning within the garnet grain*

The investigated iron- and calcium-rich garnet is characterized by smooth, continuous and concentric compositional major element transitions from core to rim (Fig. 2b and c). The observed major element variations are typical for mafic high-pressure/low temperature (HP/LT) garnets (e.g., Konrad-Schmolke et al., 2008a), such as increasing Mg and decreasing Ca and Mn contents from core to rim, as well as Fe contents that first increase towards the outer core and then decrease towards the rim. Mn shows a slight increase towards the outer rim, which is associated with a slight change in the slope of the Fe zoning. However, no abrupt or rhythmic changes nor deviations from concentric compositional patterns are visible in the major element zoning (Fig. 2b).

In contrast to the major elements, the HREEs and Y show a much more complex compositional pattern in the LA-ICP-MS maps (Fig. 3a). The heaviest REEs (Ho to Lu) and



Y have high concentrations in the centre of the crystal and show a continuous decrease across the core through c. 50% of the garnet radius. In the lighter HREEs (Tb, Dy) this central high is also developed, but is less pronounced than in the heavier HREEs. Towards the rim, the HREEs and Y show a broad annular enrichment zone that runs parallel to the euhedral edges of the garnet crystal. Rimward of this annular high, the concentrations of all HREEs greatly decrease towards the outermost rim.

Superimposed on these broad trends are rhythmic fluctuations in the REE concentrations illustrated by several concentric and roughly equally spaced peaks and associated troughs that are visible in all the HREE maps in the outer core and the annular portion of the rim (Fig. 3a). These fluctuations are also visible in profiles (Fig. 3b) that are extracted along the transect arrow shown on the Yb map. Three peaks and four associated troughs are developed in the core of the garnet (peaks denoted by arrows #1, 2 and 3 on the Tm map), two peaks and one trough are within the broad enrichment zone (arrows # 4 and 5) and at least one more peak is visible within the rim of the garnet (arrow #6). These six peaks are also marked with grey bars in Fig. 3b, which demonstrates that although relative peak heights differ among the REEs, they occur, with slight variations, at the same position for all elements. In the following section we focus on these six peaks and their associated troughs.

In addition to the profiles, chondrite-normalized REE distribution patterns (Fig. 4) were extracted from the different growth zones (peaks and troughs) evident in the REE mapping. The slopes and shapes of these REE distribution patterns reflect relative changes in REE concentrations and thus yield information about subtle geochemical changes in the host rock during garnet growth. The extracted REE distribution patterns from the troughs are clearly distinct from those of the peaks. The arrows in each panel mark the relative change of each element between the two sets (peaks and troughs) of the REE distribution patterns. For example, from the centre of the garnet to the first trough the REE distribution patterns are HREE-enriched but straight (grey lines in Fig. 4a), whereas within the first trough the REE distribution patterns show that the heaviest REEs (Ho to Lu) are preferentially depleted (black lines in Fig. 4a), leading to a slight decrease in the slope and an increase in the curvature of the patterns. This systematic difference becomes obvious if all the fluctuations are considered. Notably, peak-to-trough changes in the REE distribution patterns (Fig. 4 a, c, e, g, i and k) are associated with a fractionation of heavier REEs with respect to lighter REEs, such that the heavier REEs show a more

pronounced decrease in the troughs. In contrast, trough-to-peak changes in the REE patterns (Fig. 4 b, d, f, h j and l) are characterized by a more or less equal increase in all REEs. These recurrent changes lead to an overall change in the shape of the REE distribution patterns from linear patterns with a steep positive slope in the core towards more curved, convex upward patterns in the broad REE enrichment zone and sinusoidal patterns in the rim. Due to progressive fractionation of heavier REEs into garnet during growth, the crest of the curved REE patterns continuously shifts towards the lighter REEs.

### *Raman mapping*

A  $\mu$ -Raman map was undertaken in the same area as the REE maps prior to laser ablation analysis to visualize the distribution of the inclusion phases within the garnet. Fig. 5 shows an RGB image of the Raman mapping that illustrates the outline of the titanite and rutile inclusions within the garnet grain. The RGB channels combine the 244-262  $\text{cm}^{-1}$  (green) and 568-607  $\text{cm}^{-1}$  (red) Raman bands, which were selected to constrain the different characteristic bands for titanite and rutile. The  $\mu$ -Raman mapping shows that within the garnet core titanite is the only Ti-bearing inclusion phase, whereas in the rim rutile is present and titanite absent. Larger titanite grains outside the garnet core can only be found in the matrix and along cracks within the garnet rim and presumably reflect sample retrogression during exhumation. The Raman mapping also shows that there is a small area where rutile and titanite are both stable in a transition zone between the core and rim, which is illustrated on the Raman map by two boundaries that delimit the outermost titanites (white circles defining the white line) and innermost rutile inclusions (blue circles defining the blue line). These mineral stability fields are also plotted on top of the Lu and Ho maps (Fig. 3a) and in the extracted profiles (Fig. 3b) to demonstrate the spatial coincidence between the titanite-rutile transition as indicated by the change in the inclusion assemblage and the REE-enriched zone within the garnet crystal. The first (innermost) appearance of rutile inclusions correlates perfectly with the inner peak (peak #4) of the broad annulus, whereas the outermost occurrence of the titanite inclusions coincides well with the second peak (peak #5) of the enriched zone.

### *SIMS profiles*

Concentrations of water and the fluid mobile elements (FMEs) Li, B, F and Cl were measured by secondary ion mass spectrometry (SIMS). Mg and Ti were measured to correlate major and trace element data as well as to monitor potential titanite inclusions,

respectively. Y was monitored to correlate the FMEs with the REEs and the mapping shown in Fig. 3. SIMS measurements were performed at carefully selected spots that were free of inclusions and that represent a profile that stretches from the outer part of the central HREE high concentration zone to the annular enrichment zone in the inner garnet rim (Fig. 6). All of the FMEs as well as water show quantifiable concentrations, but only minor compositional variations that neither correlate with the REE fluctuations (peaks correspond to grey areas in Fig. 6), nor the Y pattern, nor do they correlate with each other. Water, which scatters between 50 and 80  $\mu\text{g/g}$  and F, which varies between 8 and 22  $\mu\text{g/g}$ , show slightly decreasing trends from core to inner rim, whereas Li, apart from a spike about halfway along the profile and B increase slightly from about 1 to 2  $\mu\text{g/g}$  and 30 to 70  $\mu\text{g/g}$ , respectively. Cl is relatively constant between 15 and 25  $\mu\text{g/g}$  throughout the profile. Mg, as already indicated in the EPMA measurements (Fig. 2) is constantly increasing from core to inner rim, neither correlating with the FMEs nor the REE fluctuations. Ti is constant, apart from two spikes (arrows) that might be due to the influence of titanite inclusions. These Ti spikes also show small F spikes, a slight increase in  $\text{H}_2\text{O}$  and significant Ce spikes (not shown), consistent with this interpretation.

## **Discussion and interpretation**

So far, our results demonstrate that the combination of high-resolution analytical methods, such as trace element and  $\mu$ -Raman mapping, allows for visualization of subtle trace element and mineralogical variations in two dimensions. In the following sections we demonstrate that in combination with thermodynamic geochemical modelling this integrated approach enables distinction of thermodynamic and kinetic contributions to the REE patterns in garnet. With this information it is possible to trace in great detail geochemical and geodynamic processes by investigating the trace element record stored within garnet crystals. Although, shapes and trends in trace-element growth zonation in metamorphic garnets are highly variable in detail and are influenced by variations in their trace element bulk rock chemistry or by reactions along the reaction path, REE zoning patterns in particular commonly share some very characteristic features that are also reflected in our sample. It is notable, however, that the size of our sample was about 10x10x15cm, which is not only constraining the bulk rock composition for the thermodynamic and trace element calculations but also defines the maximum extent for which our calculations, e.g. regarding rock wide equilibration or diffusion length scales,

hold true. Any larger scale processes deduced from our models are therefore based on interpolations of our results to larger length scales.

#### *The inner part of garnet REE pattern*

The inner part of the REE zoning profiles in our sample is characterized by a core enriched in HREEs followed by decreasing REE concentrations outwards (Fig. 3). This trend is visible in all HREE but with decreasing accentuation towards the lighter REEs as the height of the central peak decreases with decreasing atomic number (Fig. 3b). In our sample this central high is observable for the elements Lu to Ho, but almost invisible for the lighter REEs. Such REE patterns with high HREE concentrations in garnet cores together with a decreasing height of the central peak for the lighter REEs is common for garnets in metamorphic rocks (e.g., Skora et al., 2006) and can be simulated with a thermodynamic-geochemical model. Here we utilized Gibbs energy minimization to model mineral modes and major element compositions along a given pressure-temperature trajectory together with a mass balanced REE distribution among the modelled stable phases to calculate the resulting REE zoning in garnet (e.g., Konrad-Schmolke et al., 2008b; Konrad-Schmolke et al., 2011).

The modelled coexisting mineral assemblage along the chosen  $P$ - $T$  trajectory (Fig. 7a) during prograde garnet growth is garnet, chlorite, sodic amphibole, epidote, white mica and quartz (Fig. 7b), which is in good agreement with the evolution of natural samples from the same outcrop that have similar bulk rock compositions and similar garnet textures (Escuder-Virueite and Pérez-Estaún 2006). Over the chosen pressure and temperature interval garnet is growing between 465°C and 570°C and pressures between 1.4 and 1.9 GPa by the consumption of chlorite and epidote (Fig. 7b). The modelled shape of the major element zoning in garnet (Fig. 7c) resembles that of the natural sample supporting that the chosen  $P$ - $T$  trajectory reflects the metamorphic evolution of the sample. Quantitative differences between the modelled and observed compositions are largest in the core, where modelled Fe and Ca concentrations differ by about 15% from the observed values and modelled Mn as well as Mg differ by about 5% from the natural sample. A parameter study of the thermodynamic modelling that shows the effect of different standard state datasets and solid solution models on the results can be found in the electronic supplementary material.

447 The forward modelled core-to-rim HREE concentration profiles in garnet assuming  
448 fractional equilibrium garnet growth and mass-balanced equilibrium REE distribution  
449 among the stable phases are shown in Fig 8. The solid lines with and without circles are  
450 calculated with and without the titanite-out reaction, respectively. All the modelled  
451 profiles are characterised by an overall bell-shaped trend that is pronounced for the  
452 heavier REEs, but visible in all profiles (note that only one half of the bell is shown). These  
453 bell-shaped overall REE patterns reflect the garnet's REE concentration if the crystal is in  
454 equilibrium with an unchanged mineral assemblage, but with changing modal amounts of  
455 the reacting minerals, in this case epidote and chlorite (Fig. 7b). The different peak heights  
456 reflect the bulk distribution coefficients between garnet and the matrix minerals, whereas  
457 the broad core-to-rim decreasing trend in the HREE concentrations reflects element  
458 fractionation from the reacting bulk rock volume into the garnet crystal (e.g., Otamendi et  
459 al., 2002; Skora et al., 2006; Konrad-Schmolke et al., 2008b; Moore et al., 2013). Both of  
460 these characteristic features indicate that garnet at this stage incorporates REEs in  
461 fractional equilibrium (Moynihan and Pattison (2012) with the matrix minerals (e.g.,  
462 George and Gaidies (2017)). The continuous fractional equilibration of matrix phases with  
463 the growing garnet in our sample is exemplified by the contemporaneous change in the  
464 REE concentrations and REE distribution patterns of the titanite inclusions and the garnet  
465 crystal. The Eu/Yb ratio in titanite, reflecting the slope of the HREE distribution patterns,  
466 is increasing from the inner to the outer core (Fig. 9a) until it reaches a local maximum  
467 marked by the dashed-dotted line in Fig. 9a and b. The same trend is observed in the  
468 garnet crystal (Fig. 9b). The shallowing of the HREE distribution patterns in garnet,  
469 indicated by an increasing Eu/Yb ratio, is typical of HREE depletion in the bulk rock due  
470 to fractional garnet crystallization (e.g., Rubatto 2002) and the similarity of the pattern in  
471 titanite (change from blue to orange patterns in Fig. 9c) indicates that matrix phases, here  
472 exemplified by the titanite inclusions, also adjust to that HREE depletion in the reacting  
473 rock volume. From the local maximum marked by the dash-dotted lines towards the REE  
474 enrichment zone in garnet (stippled lines in Fig. 9a and b), the Eu/Yb ratios in titanite and  
475 garnet are decreasing and the overall REE concentration in titanite and garnet are  
476 increasing (Fig. 3 and change from orange to red patterns in Fig. 9c) as a result of the  
477 enhanced REE liberation during the titanite-out reaction. These overall changes in the  
478 REE distribution patterns as well as in the concentrations of REEs in the co-existing

titanite suggests a continuous approach to REE re-equilibration of matrix phases during garnet growth.

As the mineral assemblage during garnet growth in our example is unchanged until the breakdown of titanite, the calculated REE growth zonation follows almost exactly a Rayleigh fractionation trend in the garnet core (bold stippled line in the Lu profile in Fig. 8). This leads to a bell-shaped pattern with a broad central peak and an inflection point at about 65% of the garnet radius. However, the central peak in our sample (Fig. 3), as well as in many natural garnets (e.g. Skora et al., 2006; Corrie and Kohn 2008; George et al., 2018; Shreshta et al., 2019), is narrower than expected for a Rayleigh fractionation scenario. This can be explained by the fact that in an unchanged reacting mineral assemblage, i.e. chlorite + epidote + sodic amphibole + white mica + titanite, the width of the central peak reflects the rate with which the reacting bulk rock volume is depleted in garnet-compatible elements. The rate of bulk rock depletion is dependent on the rate of newly formed garnet and the element availability in the effective bulk rock volume (e.g., George and Gaidies 2017). This relation is demonstrated by the exemplary models shown in the Lu plot of Fig. 8. The thin solid lines display the modelled Lu zoning in garnet assuming that the effective bulk rock volume is only a fraction of the entire matrix mineral assemblage. The smaller the reacting bulk rock volume relative to the garnet growth rate, the steeper is the slope of the HREE profile in the garnet core. Transport-limited REE supply from the reacting rock volume to the garnet surface, as discussed in the next paragraph, will have the same effect and leads also to narrow central peaks with steep flanks (cf. Skora et al., 2006). It has been shown, however, that garnet growth rates can vary during a rock's metamorphic evolution (e.g., George and Gaidies 2017) and that deviations from fractional equilibrium major and trace element incorporation during garnet growth occur (e.g., Carlson 2002), which implies that in order to quantify the extent of thermodynamic equilibrium in a rock volume a representative number of garnet porphyroblasts has to be investigated in detail (e.g., George and Gaidies 2017; Gaidies et al., 2008; Gaidies et al., 2018).

In general the widths and slopes of the bell-shaped HREE central peaks in natural garnets are constrained by the endmember scenarios of (1) fractional equilibrium crystallisation, if the garnet grows in fractional equilibrium with the entire matrix, (2) partial equilibration with matrix phases if only parts of the matrix phases equilibrate with the growing garnet and (3) transport-limited REE supply. Natural samples will likely reflect

a combination of these scenarios, but shapes and widths of the central peaks can be used to qualitatively constrain the bulk element permeability of the interconnected transport matrix (ITM). Small to moderate amounts of garnet growing in fractional equilibrium with a large reacting rock volume, such as often observed in felsic rocks, will develop a zonation similar to a Rayleigh fractionation profile (e.g., Otamendi et al., 2002; Moore et al., 2013; Gieré et al., 2011). In contrast, large garnet porphyroblasts with limited REE supply from matrix phases, such as in our metamafic sample, will more rapidly deplete the reacting rock volume and develop a narrower and steeper central peak.

#### *The effect of titanite breakdown on the REE zonation*

Towards the rim of the natural garnet crystal, the bell-shaped REE trend is reversed and most REEs start to increase and form an annular enrichment zone. Such an enrichment zone following the bell-shaped pattern in the garnet core is also a common feature seen in REE profiles in metamorphic garnets from different rock types and different tectonic settings (e.g., Skora et al., 2006; Usui et al., 2007; Corrie and Kohn 2008; Gieré et al., 2011; George and Gaidies 2018; Shreshta et al., 2019; Rubatto et al., 2020). As indicated by the correlation between the  $\mu$ -Raman and REE mapping (Figs. 3 and 5), the reversals in the trends of all HREEs that form the broad overall enrichment zone in our sample can be linked to titanite breakdown and the growth of rutile in the sample. In contrast to rutile that usually contains no or only negligible amounts of REEs (e.g., Meinhold 2010), titanite is an REE-bearing phase (e.g., Garber et al., 2017) and the REEs liberated by the titanite breakdown are thus incorporated into garnet during this reaction. This clear coincidence is interpreted to indicate that the reaction where titanite breaks down to form rutile is associated with the broad zone of REE enrichment at the core-rim transition in the garnet crystal.

In order to model the effect of titanite breakdown on the REE pattern in garnet, titanite stability was superimposed on the thermodynamic calculations and its breakdown was simulated with an Avrami-type reaction progress between 541°C at 1.72 GPa and 556°C at 1.79 GPa (Fig. 6a and b). Superimposed titanite breakdown was preferred over the thermodynamic simulation of Ti-phases as the experimental data on the titanite-rutile transition are limited (Manning and Bohlen 1991; Angiboust and Harlov 2017). Further, the published data on the titanite-rutile transition suggest a strong dependence on the bulk rock composition (Angiboust and Harlov 2017). Furthermore, the thermodynamic data on Ti incorporation in major phases, such as amphibole, pyroxene and white mica

are mostly unknown and the incorporation of Ti into thermodynamic calculations requires knowledge of the oxygen fugacity during the rock's metamorphic evolution due to the interplay of iron oxides and ilmenite. Lastly, we believe that neither titanite nor rutile have a significant influence on the major phase assemblage.

The narrow REE hump in the modelled profiles between about 70 and 90% of the garnet radius (Fig. 8) results from titanite breakdown. The effect of the titanite-out reaction on the REE uptake is best demonstrated by a comparison with the modelled curves calculated without titanite breakdown (bold solid lines in Fig. 8). Controlled by the REE partition coefficients, the titanite-out reaction leads to an increase in the HREE (Dy to Lu), but not in REEs lighter than Dy. Titanite typically has flat or negatively-sloped HREE patterns (Scibiorski et al., 2019, Fig. 9) so that the difference in peak heights cannot be related to the REE composition of the titanites, but rather to the combined effect of REE liberation and garnet/bulk rock distribution coefficients.

Several studies have shown that other distinct mineral reactions, such as the breakdown of major phases (amphibole, epidote; Konrad-Schmolke et al., 2008), of accessory phases (allanite, monazite, xenotime, ilmenite, titanite; Pyle and Spear 1999; Gieré et al., 2011; Gaidies et al., 2021; this work) or the resorption of earlier grown garnet (e.g., Kulhanek et al., 2021) can also lead to such an annular increase in the REEs. Characteristic for this stage of equilibrium REE uptake in garnet is that the enrichment peaks for all REEs occur at the same position within the garnet crystal if the REE-liberating phase breakdown occurs over a small garnet growth interval (e.g., Moore et al., 2013). Nevertheless, the enrichment peaks can vary slightly in their positions for different REEs if the REE-liberating reaction is continuous and occurring over a larger garnet growth interval. In that case the reactants might be able to equilibrate with respect to their REE content during the reaction progress, as demonstrated in Fig. 7, and fractionation of HREE over LREE might occur due to the continuous equilibrium REE distribution between reactants and garnet. Hence, in that case HREEs might be earlier incorporated than LREEs, which are continuously held back in the reactants (e.g., Konrad-Schmolke et al., 2008b). However, this effect must not be misinterpreted as diffusion-controlled REE incorporation (cf. Skora et al., 2006), which will be discussed in the following paragraphs.

It should be noted, however, that it might be difficult to unambiguously determine the reactant minerals simply from the reaction-controlled REE enrichment in garnet, if the sample does not preserve such a detailed inclusion assemblage as in our case. This is



because the REE concentrations as well as the REE distribution patterns in the reacting minerals control the shape and intensity of the resulting REE increase as well as the resulting REE distribution patterns in the coexisting garnet (cf. Konrad-Schmolke et al., 2008b). Hence, reactants with similar REE contents, such as for example apatite, epidote or lawsonite, might leave similar REE signatures in the co-existing garnet.

#### *The REE fluctuations – recurring variation in rock permeability*

Superimposed on the afore described broad REE pattern in our sample are distinct recurring smaller peaks at fixed positions relative to the garnet radius that are developed to different extents but are visible in the profiles of all REEs. This is a feature that often occurs in the REE patterns of metamorphic garnet (e.g., Skora et al., 2006; Moore et al., 2013; George and Gaidies 2018; this work), but is often undetected as it requires a high spatial resolution of the analytical spots or even REE mapping to be visualized properly. REE mapping from our sample show that these recurring smaller peaks (peaks 1 – 6) are indeed annular features (Fig. 3a) that occur at fixed positions (Fig. 3b), which rules out analytical artifacts to be the reason for the slight REE variations. These compositional fluctuations (peaks and troughs) superimposed on the broad REE zoning pattern in our sample offer the possibility to extract further detailed information about variations in the rock element transport properties and permeabilities.

Repetitive compositional variations, such as oscillatory zoning, in metamorphic garnet has been attributed to several geodynamic and kinetic parameters. They have been interpreted, for example, to be the result of rhythmic variations of pressure and temperature during garnet growth (Kohn 2004; Stowell et al., 2011; Viete et al., 2018), but more likely to reflect garnet growth rate variations (e.g., George and Gaidies 2017) or changes in the element supply such as by varying fluid fluxes (e.g., Jamtveit et al., 1993; Jamtveit and Hervig 1994; Clechenko and Valley 2003; Dziggel et al., 2009; Zhai et al., 2014; Ranjbar et al., 2016). In the following we will discuss these aspects in detail.

#### *Pressure and/or temperature variations*

Rhythmic variations in pressure and/or temperature are very unlikely reflected in the compositional variations of our garnet crystal. Garnet major element composition is very sensitive to pressure and temperature changes, which makes it a versatile mineral regarding geothermobarometry. Hence, slight variations, especially fluctuating variations in pressure and/or temperature will result in rhythmic variations in the major element

composition of garnet, such as demonstrated in Kohn et al., 2004 and Viete et al., 2018. In our sample major element patterns (Fig. 2) display smooth and continuous changes from core to rim. We take the preservation of significant fluctuations in fast diffusing elements, such as Li (Fig. 6), as evidence for the assumption that the smooth major element zonations are actually growth zonations and that extensive diffusional equilibration did not occur during the sample's exhumation. Hence, the absence of major element fluctuation that correspond with the REE variations (Fig. 6) excludes pressure and/or temperature fluctuations as the cause of the REE fluctuations in our sample.



#### Garnet growth rate variations

However, it is more difficult to decide whether garnet growth rate variations or changing fluid fluxes are the cause for the REE fluctuations. If element transport in the ITM is sluggish and REE incorporation at the garnet surface is potentially transport-controlled, growth rate variations will lead to varying REE depletion halos around the growing porphyroblasts (e.g., George and Gaidies 2018). At times of enhanced garnet growth, the higher demand of REEs will, at constantly sluggish element fluxes in the ITM, lead to enhanced depletion of slowly diffusing elements in the ITM surrounding the growing garnet (cf. Carlson 1989; Chernoff and Carlson 1997; Meth and Carlson 2005; Skora et al., 2006). This will in turn lead to decreasing REE concentrations at the garnet surface. At times of slow garnet growth element transport might keep pace again with the demand at the garnet surface and REE concentration in garnet will increase. On the other hand, the same effect on REE variations in garnet will occur if, at constant garnet growth, the element supply is changing due to fluctuations in the ITM permeability, such as by varying fluid fluxes through the host rock. Hence, the two processes, which might even be interconnected, will have the same effect on the REE pattern in garnet.

Nevertheless, one striking argument against significant growth rate fluctuations during the formation of the garnet core in our sample is the homogeneous distribution of the numerous fine-grained inclusions. Matrix phases are included in porphyroblasts if the advancement of the growing surfaces is preferred over the energetic equilibration of the surface energies between matrix phases and the growing crystal. Therefore, slowly growing phases are more likely to contain fewer inclusions, whereas poikiloblastic grains are interpreted to be the result of rapid crystal growth. Consequently, growth rate variations in our sample should be reflected in a concentrically changing inclusion density pattern, as it is observed if the garnet core and the rim of our sample are compared. Within

the core, however, the inclusions are very homogeneously distributed, pointing towards a potentially rapid, but constant advancement of the garnet surfaces throughout the growth of the garnet core.

#### Changing fluid chemistry

Especially in settings with high fluid throughput, such as in hydrothermal systems like skarns or, as in the case of our sample, in subduction zones, where chemically contrasting rocks are tectonically juxtaposed, rapidly changing fluid compositions might be expected. Such variations in fluid chemistry might include the concentration of REEs (e.g., Dziggel et al., 2009) and other trace elements (e.g., Jamtveit et al., 1993), the oxygen fugacity ( $f_{O_2}$ ) as well as changes in salinity or pH (e.g., Zhai et al., 2014). Although fluid chemistry changes cannot be ruled out completely to be the reason for the REE fluctuations, some of the observations in our sample rather suggest relatively constant chemical conditions in the fluid. First of all, water concentrations are constantly between 50 and 80  $\mu\text{g/g}$ , which suggests that an aqueous fluid is always present during garnet growth (Fig. 6). The concentrations of the FMEs in this fluid are relatively constant and none of the minor fluctuations in FME concentration correlates with the observed REE variations (Fig. 6). Chlorine is also relatively constant indicating only minor changes in fluid salinity. Hence, even if changes in fluid chemistry occurred and are represented in the minor fluctuations of the fluid mobile elements, they did not affect the REE distribution in the garnet. Also,  $f(O_2)$ , a factor that could influence the REE distribution coefficients (e.g., Dalpé and Baker 2000) was likely constant at least during the growth of the garnet interior. This is indicated by the  value that is shown in the map in Fig. 9d.  is relatively constant around 0.9 (orange colours) in the garnet core until the annular REE enrichment zone. Only the rim of the garnet shows significantly different values that reach up to 1.2 (red colours) indicating lower  $f(O_2)$  with progressive subduction.

#### Changing element transport properties in the host rock

Evidence for changing element transport properties of the host rock during garnet growth results from the investigation of the REE distribution patterns in the garnet crystal. Garnet prefers HREEs over LREEs with a broadly linear relationship on a chondrite-normalized REE distribution diagram, and hence typical REE distribution patterns in garnet are straight with a steep positive slope when plotted with increasing atomic number (e.g., the grey REE spectra from the garnet core in Fig 4a). Convex upward curved REE distribution

patterns, such as in Fig. 4l, indicate HREE depletion of the reacting rock as a result of element fractionation into the growing garnet (e.g., Otamendi et al., 2002). This effect is more pronounced with smaller reacting rock volumes, hence the change in curvature of the REE distribution patterns is indicative of the size of the equilibration volume around the growing garnet.

The REE distribution patterns extracted from the troughs and peaks of the fluctuations differ systematically. The REE distribution patterns in all troughs show a preferred fractionation of heavier versus lighter REEs (Fig. 4 a, c, e, g, i and k), indicated by stronger concave downward curvature compared to the associated peaks. This difference is clearly indicative of the enhanced removal of HREEs from a smaller reacting bulk rock volume during trough growth compared to the larger equilibration volumes during peak formation. In turn, this can be interpreted as reflecting the presence of a compartmentalized ITM, which might be for example a non-interconnected fluid-filled pore space during the development of the troughs. Slow REE transport in a stagnating fluid column together with ongoing garnet growth and fractional crystallization leads to rapid REE depletion in the reduced ITM volume and the development of concentration gradients around the garnet crystal, which in turn is reflected in the strong fractionation of heavier REEs with respect to lighter REEs during trough development.

In contrast, the curvature of the REE distribution patterns does not change during the development of the fluctuation peaks (Fig. 4b, d, f, h j and l), which indicates a limited fractionation effect and hence an increasing equilibration volume during peak development. It is therefore likely that at these growth stages garnet is in equilibrium with a larger rock volume, suggesting that the ITM is interconnected and allows for effective trace element (REE) transport. Hence, during the growth of the “peak” zones, all REEs are equally replenished, whereas during growth stages with decreasing REE concentrations (the troughs) the supply of heavier REEs could not keep pace with growth resulting in a more convex upward REE distribution pattern. These observations demonstrate that the development of the REE fluctuations superimposed on the broad overall REE pattern in the garnet are likely caused by changing rock permeabilities and therefore changing REE transport properties.

*A conceptual model of garnet growth*

In order to support this conceptual model we use a simplified numerical approach to model the qualitative effect of limited REE supply from a restricted rock volume on the garnet REE zonation. We simulate the development of a concentration gradient around the garnet crystal by superimposing diffusion-limited REE uptake at the garnet surface on the fractional equilibrium model. For this approach we superimposed a Crank-Nicolson finite difference diffusion model on the incremented thermodynamic-geochemical calculations. For the diffusion simulation the amount of step increments on the reaction path was reduced to 20 increments for the diffusion-limited model (every 10<sup>th</sup> increment of the original *P-T* trajectory). Each of the 20 increments was then again segmented into 100 equally spaced elements on which the Crank-Nicolson finite difference method was applied. As explained in the electronic supplementary material, we set the time increment to 200 years and the spatial increment to 0.025 mm. Volume diffusion within the garnet crystal was neglected. Intercrystalline REE diffusion was modelled assuming a system size of 10 mm and an Arrhenius-type function for the calculation of the diffusion coefficient  $D = D_0 \exp^{-Q/RT}$ . We used a value of  $D_0 = 2.8 \times 10^{-5} \text{ cm}^2/\text{a}$  for the pre-exponential factor (cf. Skora et al., 2006) and an activation energy of 30 kJ/mol for intercrystalline Lu diffusion. Modelling of the diffusion-controlled REE uptake starts at each calculated increment with the REE concentration defined by the fractional equilibrium REE distribution calculations. Between two increments of the diffusion model the flux of REE from the surrounding matrix towards the garnet surface is calculated assuming the above-mentioned diffusion parameters. After each calculated diffusion-limited growth interval, the REE concentration at the garnet surface returns to the value calculated for fractional equilibrium crystallization. A detailed description of the algorithm is given in the electronic supplementary material.

The modelled Lu concentration in garnet assuming fractional equilibrium garnet growth and mass-balanced equilibrium REE distribution among the stable phases is demonstrated by the bold black line in Fig. 10a. This is the same profile as in Fig. 8 and represents the garnet's Lu concentration for fractional equilibrium with the matrix minerals. A similar curve can also be drawn enveloping the Lu profile of the natural sample (solid black line on Fig. 10b). As discussed above, this curve reflects the maximum Lu concentration the garnet can achieve in its respective growth environment. In the modelled case (Fig. 10a) this is the fractional equilibrium with the entire rock volume as well as with the reacting titanite during the development of the annular REE increase. In

case of the natural sample (Fig. 10b), where the central peak is narrower, hence the equilibration volume might be smaller, this curve can be seen as the maximum Lu concentration the garnet can achieve in a certain background REE flux.

However, in order to explain the REE fluctuations superimposed on this broad pattern, seven segments of the  $P$ - $T$  trajectory are shown where periods of diffusion-limited intercrystalline REE transport towards the garnet surface are simulated with our simplified Crank-Nicolson approach (Fig. 10a). Diffusion-limited REE supply leads to a decrease of the REE concentration relative to the fractional equilibrium concentration at the garnet surface (thin black line in Fig. 10a). After each calculated interval of diffusion-limited REE supply the REE concentration at the garnet surface returns to the value calculated for fractional equilibrium crystallization leading to the saw-tooth pattern shown by the thin black curves in Fig. 10a. The red curve in Fig. 10a displays a concentration profile resulting from the fluctuating interplay of fractional equilibrium REE incorporation and diffusion-limited REE uptake, thus reflecting fluctuating rock permeabilities during garnet growth. This modelled curve mimics the REE fluctuations measured in our sample given by the solid red line in Fig. 10b.

The different effects of fractional equilibrium and kinetically controlled garnet growth in our sample can be summarized in the conceptual model shown in Fig. 11, which involves three fundamental steps:

(1) Garnet growth starts in equilibrium with a rock volume that has a background permeability allowing for a certain continuous element flux (Fig. 11a, left panel, physical process). REE incorporation into garnet follows fractional equilibrium crystallization controlled by modal changes of matrix minerals in the host rock (Fig. 11a, middle panel, chemical process). This background element flux is enabled by an interconnected and potentially fluid-filled pore space in the ITM. The REE concentration in garnet follows the bold black line in Fig. 10a and in the right panel of Fig. 11a. The equilibration among garnet and (at least fractions of) matrix phases in the natural sample is demonstrated by the simultaneous change in REE concentrations and REE distribution patterns in garnet and titanite (Fig. 6). A rock-wide elemental equilibration at this stage of garnet growth is likely facilitated by the availability of a free fluid phase as an element transport medium at the early stages of metamorphism.

(2) The permeability of the rock is decreasing, for example due to burial- or reaction-induced compaction and/or fluid drainage (e.g. Balashov and Yardley 1998; Connolly 2010), which leads to the closure of parts of the pore space and to compartmentalization of the reacting rock volume (Fig. 11b, left panel). Decreasing rock permeability shuts off fluid percolation, hinders element equilibration and leads to a strongly transport-controlled REE incorporation into the growing garnet. Garnet growth at this stage causes a rapid REE decrease in the compartmentalized ITM as well as at the garnet surface (Fig. 11b, middle panel), which leads to the development of the observed REE troughs (Fig. 11b, right panel). The pronounced fractionation of heavier REE over lighter REEs associated with the trough development (Fig. 4) further supports the arguments for this process.

(3) Rock permeability increases until the pore space becomes interconnected again (Fig. 11c, left panel), e.g., due to ongoing devolatilization reactions in the host rock, which elevate the pore fluid pressure (e.g., Connolly 1997; Oliver and Bons 2001; Taetz et al., 2018; Marti et al., 2021), or due to changing external stressed, that might cause various forms of dilatancy (e.g., Sibson 1994; Füsseis et al., 2009; Viete et al., 2018). The increasing permeability allows for increasing fluid percolation and faster element transport in the rock, which facilitates REE transport and replenishes the REE budget available for the growing garnet (Fig. 11c, middle panel). REE concentration in garnet returns to that of the initial continuous background element flux (Fig. 11c, right panel) without significant fractionation of heavier over lighter REEs as observed during peak development (Fig. 4).

Recurrence of these three process steps together with the titanite-to-rutile transition eventually leads to the development of the observed complex REE zonation patterns and REE distribution pattern in our sample (Fig. 11d, right panel). Nevertheless, we point out that the diffusion models are used to demonstrate the feasibility of our conceptual model and that more data on REE diffusion in fluids as well as more sophisticated model approaches are needed to derive quantitative data from this approach. This, however, is beyond the scope of this paper.

#### *Application to other natural samples*

The combination of our natural observations with the above thermodynamic-geochemical model together with the consideration of published examples demonstrate that the broad shape of REE zoning patterns often observed in metamorphic garnets, i.e.

a bell-shaped REE pattern with decreasing central peak height for decreasing atomic number in the garnet cores, followed by an annular REE enrichment zone, is the result of a change from fractional equilibrium REE uptake during garnet growth in an unchanged matrix mineral assemblage, to a reaction controlled REE uptake during the breakdown of major and/or accessory phases, such as demonstrated in Moore et al., (2013). Hence, such typical REE patterns can be used to infer the reaction path of the host rock (e.g., Konrad-Schmolke et al., 2008; Moore et al., 2013).

In contrast, the kinetic aspects of garnet formation are reflected in the widths and shapes of the central peaks as well as in recurring slight variations in the HREE concentrations that are superimposed on the general trend. These HREE fluctuations reflect the formation of depletion halos around the growing garnet and are therefore the expressions of recurring kinetic barriers that change the length scales of equilibration for the HREE in the ITM. We interpret the fluctuating occurrence of these peaks to be the result of changing interconnectivities of the ITM, hence indicating changes in the rock's element transport properties. As these fluctuations are common in metamorphic garnet, especially in high-pressure samples, it is likely that fluctuations in the element transport properties in metamorphic rocks, especially in subduction zones, are also common. The general reason for that can be that pulse-like fluid production and migration is a common process during metamorphism (e.g., Pollington and Baxter 2011; Connolly and Podlachikov 2013).

#### *Lateral peak shifts: diffusion- or reaction-controlled?*

Another often observed, but yet not fully explained, feature in REE patterns of metamorphic garnets is a significant lateral shift of the REE annuli, that are resulting from a reaction-controlled REE uptake, towards more outward positions with decreasing atomic number. This feature has first been described by Skora et al., (2006) and is interpreted to be the result of transport-controlled element supply and strongly different diffusion velocities for HREE and LREE. Konrad-Schmolke et al., (2008b) interpreted this peak shift to be caused by fractional incorporation of REEs into garnet during reactions that occur over a larger pressure and temperature interval, such that heavier REEs are primarily incorporated into garnet at the onset of the reaction, whereas lighter REEs are held back in the reacting phases as dictated by the distribution coefficients of reactants and garnet. This would be the case if reactants and garnet are in thermodynamic equilibrium and the reactant composition is constantly equilibrated, for example due to



recrystallisation, and continuously depleted in HREEs over LREEs. However, in our example such a peak shift is exemplified by the observation that the peaks 4 and 5 in Figs. 3 and 4, that result from the titanite breakdown reaction, are changing in their relative heights, which shifts the peak of the reaction-induced REE enrichment zone towards more outward positions for the lighter REEs. Furthermore, peak 5 and peak 6 in Figs. 3 and 4 are also slightly shifted outward with decreasing atomic number of the REE. Regarding the formation of peak 5 it is very unlikely that the peak shift is caused by different diffusive properties of HREEs and LREEs as the transport distance between reactants (titanite) and product (garnet) is negligible. On the other hand, a reaction-induced fractionation of HREE over LREE is not observed, as shown in Fig. 9. A HREE depletion in the reactants and/or a preferential incorporation of LREE in the refractory reactants can therefore not be the case for the shift of peak 5. Nevertheless, the remaining titanite still seems to be equilibrated with the garnet during the reaction as indicated by the homogeneous replenishment of REEs in titanites from the outer core towards the reaction zone (Fig. 9b), a feature that is also observed in the garnet during the development of the REE peaks (Fig. 4). Hence, the observations in our sample cannot unambiguously distinguish between the different scenarios, but rather yield arguments for both aspects. It has to be noted, however, that a peak shift in our sample is only observed in the outermost parts of the garnet, when garnet growth likely occurred at conditions with a limited fluid supply and reduced element transport capacities of the host rock, as with ongoing subduction the rock continuously dehydrates and fluid liberation gradually ceases. Furthermore, as indicated by the recurring REE fluctuations, periods of a transport-limited element supply are evident during garnet growth.

Data constraining the intercrystalline REE transport in metamorphic rocks do not exist, but in a few cases differences in diffusion velocities between LREE and HREE are reported. LREE volume diffusion seems to be significantly slower than HREE volume diffusion in pyroxenes (Van Orman et al., 2001) and, more important for the interpretation of our data, LREE diffuse also slower than HREE during grain boundary diffusion in metal alloys (Loewe et al., 2017; Higashino et al., 2019). Hence, one could argue that the lateral shifts in REE annuli at the outermost parts of metamorphic garnets are developed in a setting with very limited fluid supply where grain boundary diffusion is the dominant REE transport mechanism. A conceptionally sound model that clarifies the processes that lead to such lateral peak shifts must still be developed as this feature poses an integral

question towards the full understanding of REE zonation patterns and their interpretation in terms of geodynamic and geochemical processes during garnet growth in metamorphic rocks.

## **Conclusions**

A detailed mineralogical and chemical study of a single garnet grain in a high-pressure metamorphic sample from the Samana peninsula (Dominical Republic) yields insight into the reaction path as well as into the chemical and physical changes during the rock's metamorphic evolution. Based on combined two-dimensional REE and  $\mu$ -Raman mapping together with thermodynamic-geochemical modelling, a detailed interpretation of the REE variations within the garnet crystal in terms of thermodynamic and kinetic contributions to the REE growth zonation is possible. The overall bell-shaped REE growth zonation observed in the investigated garnet grain reflect fractional garnet crystallization in an unchanged matrix phase assemblage. Differing heights of the central peaks for the different REEs are caused by fractionation of HREE over LREE into the growing garnet dictated by the garnet/bulk rock distribution coefficients. Peak widths and slopes of the peak flanks are controlled by the background REE supply from the matrix assemblage to the garnet surface, which is influenced by the fraction of matrix phases the garnet is in equilibrium with as well as by the overall transport properties of the interconnected transport matrix. A pronounced annular increase in HREE towards the rim of the garnet crystal reversing the overall bell-shaped compositional trend can be attributed to the titanite-out reaction that liberates significant amounts of HREE that cannot be incorporated into newly-formed rutile during titanite breakdown. Superimposed on the bell-shaped growth zonation are also recurring REE fluctuations that can be visualized with the trace element mapping. These REE fluctuations might reflect recurring changes in the rock's element transport permeabilities associated with varying fluid fluxes through the host rock during garnet growth. Our results further demonstrate that 2-D trace element and  $\mu$ -Raman mapping yield a plethora of new information that is crucial for future interpretations of complex compositional growth zonation in metamorphic minerals.

## **Acknowledgements**

The authors thank Christine Fischer for thin section preparation and Thomas Zack and Nils Gies for fruitful discussions that significantly improved the manuscript. Funding of

this work by the Deutsche Forschungsgemeinschaft (grant KO-3750/3) is gratefully acknowledged. We thank two anonymous reviewers as well as Fred Gaidies and Tetsuo Kawakami for their thorough work and helpful comments and suggestions that improved the manuscript. Katy Evans is thanked for the thorough editorial handling, including important comments that also improved the quality of the text. SIMS analyses were supported by a NERC IMF pilot grant to Ralf Halama. David Chew acknowledges past and present support from Science Foundation Ireland (SFI) through research grants 12/IP/1663, 15/IA/3024, 13/RC/2092 and 13/RC/2092\_P2 (iCrag Research Centre). iCrag is funded under the SFI Research Centres Programme. The authors declare to have no potential sources of conflict of interest.

## References

- Angiboust, S., and Harlov, D. (2017). Ilmenite breakdown and rutile-titanite stability in metagranitoids: Natural observations and experimental results. *American Mineralogist*, 102(8), 1696-1708.
- Balashov, V. N. and Yardley, B. (1998). Modeling metamorphic fluid flow with reaction-compaction permeability feedbacks. *American Journal of Science*, 298, 441-470.
- Baldwin J.A., Powell, R., Brown, M., Moraes, R and Fuck, R. A., 2005. Modelling of mineral equilibria in ultrahigh-temperature metamorphic rocks from the Anapolis-Itaçu Complex, central Brazil. *Journal of Metamorphic Geology*, 23, 511-531.
- Caddick, M. J., Konopásek, J., and Thompson, A. B. (2010). Preservation of garnet growth zoning and the duration of prograde metamorphism. *Journal of Petrology*, 51(11), 2327-2347.
- Carlson, W. D. (1989). The significance of intergranular diffusion to the mechanisms and kinetics of porphyroblast crystallization. *Contributions to Mineralogy and Petrology*, 103(1), 1-24.
- Carlson, W.D., 2002. Scales of disequilibrium and rates of equilibration during metamorphism. *American Mineralogist*, 87(2-3), pp.185-204.
- Carlson, W. D. (2006). Rates of Fe, Mg, Mn, and Ca diffusion in garnet. *American Mineralogist*, 91(1), 1-11.
- Carlson, W. D. (2012). Rates and mechanism of Y, REE, and Cr diffusion in garnet. *American Mineralogist*, 97(10), 1598-1618.

931 Catlos, E. J., and Sorensen, S. S. (2003). Phengite-based chronology of K-and Ba-rich fluid  
 932 flow in two paleosubduction zones. *Science*, 299(5603), 92-95.

933 Chernoff, C. B., and Carlson, W. D. (1997). Disequilibrium for Ca during growth of pelitic  
 934 garnet. *Journal of Metamorphic Geology*, 15(4), 421-438.

935 Clechenko, C. C., and Valley, J. W. (2003). Oscillatory zoning in garnet from the Willsboro  
 936 Wollastonite Skarn, Adirondack Mts, New York: a record of shallow hydrothermal  
 937 processes preserved in a granulite facies terrane. *Journal of Metamorphic Geology*, 21(8),  
 938 771-784.

939 Connolly, J. A. D. (1997). Devolatilization-generated fluid pressure and deformation-  
 940 propagated fluid flow during prograde regional metamorphism. *Journal of Geophysical*  
 941 *Research: Solid Earth*, 102(B8), 18149-18173.

942 Connolly, J. A. (2010). The mechanics of metamorphic fluid expulsion. *Elements*, 6(3),  
 943 165-172.

944 Connolly, J. A. D., and Podladchikov, Y. Y. (2013). A hydromechanical model for lower  
 945 crustal fluid flow. In *Metasomatism and the chemical transformation of rock* (pp. 599-  
 946 658). Springer, Berlin, Heidelberg.

947 Corrie, S. L., and Kohn, M. J. (2008). Trace-element distributions in silicates during  
 948 prograde metamorphic reactions: Implications for monazite formation. *Journal of*  
 949 *Metamorphic Geology*, 26(4), 451-464.

950 de Capitani, C., and Brown, T. H. (1987). The computation of chemical equilibrium in  
 951 complex systems containing non-ideal solutions. *Geochimica et Cosmochimica*  
 952 *Acta*, 51(10), 2639-2652.

953 Dalpé, C. and Baker, D.R., 2000. Experimental investigation of large-ion-lithophile-  
 954 element-, high-field-strength-element-and rare-earth-element-partitioning between  
 955 calcic amphibole and basaltic melt: the effects of pressure and oxygen  
 956 fugacity. *Contributions to Mineralogy and Petrology*, 140(2), pp.233-250.

957 Dziggel, A., Wulff, K., Kolb, J., Meyer, F. M., and Lahaye, Y. (2009). Significance of  
 958 oscillatory and bell-shaped growth zoning in hydrothermal garnet: Evidence from the  
 959 Navachab gold deposit, Namibia. *Chemical Geology*, 262(3-4), 262-276.

960 Escuder-Virueite, J., and Pérez-Estaún, A. (2006). Subduction-related P–T path for  
 961 eclogites and garnet glaucophanites from the Samana Peninsula basement complex,  
 962 northern Hispaniola. *International Journal of Earth Sciences*, 95(6), 995-1017.

963 Escuder-Virueite, J., Pérez-Estaún, A., Gabites, J., and Suárez-Rodríguez, Á. (2011a).  
 964 Structural development of a high-pressure collisional accretionary wedge: the Samaná  
 965 complex, northern Hispaniola. *Journal of Structural Geology*, 33(5), 928-950.

966 Escuder-Virueite, J., Pérez-Estaún, A., Booth-Rea, G., and Valverde-Vaquero, P. (2011b).  
 967 Tectonometamorphic evolution of the Samaná complex, northern Hispaniola:  
 968 implications for the burial and exhumation of high-pressure rocks in a collisional  
 969 accretionary wedge. *Lithos*, 125(1-2), 190-210.

970 El Korh, A., 2010. Geochemical fingerprints of devolatilization reactions in the high-  
 971 pressure rocks of Ile de Groix, France (Doctoral dissertation, University of Geneva).

972 Fusseis, F., Regenauer-Lieb, K., Liu, J., Hough, R.M. and De Carlo, F., 2009. Creep  
 973 cavitation can establish a dynamic granular fluid pump in ductile shear  
 974 zones. *Nature*, 459(7249), pp.974-977.

975 Gaidies, F., Abart, R., De Capitani, C., Schuster, R., Connolly, J.A.D. and Reusser, E., 2006.  
 976 Characterization of polymetamorphism in the Austroalpine basement east of the Tauern  
 977 Window using garnet isopleth thermobarometry. *Journal of Metamorphic Geology*, 24(6),  
 978 pp.451-475.

979 Gaidies, F., De Capitani, C. and Abart, R., 2008. THERIA\_G: a software program to  
 980 numerically model prograde garnet growth. *Contributions to Mineralogy and*  
 981 *Petrology*, 155(5), pp.657-671.

982 Gaidies, F., Petley-Ragan, A., Chakraborty, S., Dasgupta, S. and Jones, P., 2015.  
 983 Constraining the conditions of Barrovian metamorphism in Sikkim, India: P–T–t paths of  
 984 garnet crystallization in the Lesser Himalayan Belt. *Journal of Metamorphic*  
 985 *Geology*, 33(1), pp.23-44.

986 Gaidies, F., Morneau, Y.E., Petts, D.C., Jackson, S.E., Zagorevski, A. and Ryan, J.J., 2021.  
 987 Major and trace element mapping of garnet: Unravelling the conditions, timing and rates  
 988 of metamorphism of the Snowcap assemblage, west-central Yukon. *Journal of*  
 989 *Metamorphic Geology*, 39(2), pp.133-164.

990 Ganguly, J., Cheng, W., and Tirone, M. (1996). Thermodynamics of aluminosilicate garnet  
 991 solid solution: new experimental data, an optimized model, and thermometric  
 992 applications. *Contributions to Mineralogy and Petrology*, 126(1-2), 137-151.

993 Garber, J. M., Hacker, B. R., Kylander-Clark, A. R. C., Stearns, M., and Seward, G. (2017).  
 994 Controls on trace element uptake in metamorphic titanite: Implications for  
 995 petrochronology. *Journal of Petrology*, 58(6), 1031-1057.

996 George, F. R., and Gaidies, F. (2017). Characterisation of a garnet population from the  
 997 Sikkim Himalaya: insights into the rates and mechanisms of porphyroblast  
 998 crystallisation. *Contributions to Mineralogy and Petrology*, 172(7), 57.

999 George, F.R., Gaidies, F. and Boucher, B., 2018. Population-wide garnet growth zoning  
 1000 revealed by LA-ICP-MS mapping: implications for trace element equilibration and syn-  
 1001 kinematic deformation during crystallisation. *Contributions to Mineralogy and*  
 1002 *Petrology*, 173(9), pp.1-22.

1003 Gieré, R., Rumble, D., Günther, D., Connolly, J., and Caddick, M. J. (2011). Correlation of  
 1004 growth and breakdown of major and accessory minerals in metapelites from  
 1005 Campolungo, Central Alps. *Journal of Petrology*, 52(12), 2293-2334.

1006 Gleeson, M. L. M., Gibson, S. A., Stock, M. J., and EIMF (2022). Constraints on the  
 1007 behaviour and content of volatiles in Galápagos magmas from melt inclusions and  
 1008 nominally anhydrous minerals. *Geochimica et Cosmochimica Acta* 319, 168-190.

1009 Goncalves, P., Guillot, S., Lardeaux, J. M., Nicollet, C., and Mercier de Lepinay, B. (2000).  
 1010 Thrusting and sinistral wrenching in a pre-Eocene HP-LT Caribbean accretionary wedge  
 1011 (Samaná Peninsula, Dominican Republic). *Geodinamica acta*, 13(2-3), 119-132.

1012 Hermann, J. (2002). Allanite: thorium and light rare earth element carrier in subducted  
 1013 crust. *Chemical geology*, 192(3-4), 289-306.

1014 Higashino, F., Kawakami, T., Tsuchiya, N., Satish-Kumar, M., Ishikawa, M., Grantham, G., Sakata, S.,  
 1015 & Hirata, T. (2019). Brine Infiltration in the Middle to Lower Crust in a Collision Zone: Mass  
 1016 Transfer and Microtexture Development Through Wet Grain-Boundary Diffusion. *Journal of*  
 1017 *Petrology*, 60(2), 329-358.

1018 Holland and Powell (1996) Thermodynamics of order-disorder in minerals: II.  
 1019 Symmetric formalism applied to solid solutions. *American Mineralogist*, 81, 1425-1437.

1020 Holland, T. J. B., and Powell, R. T. J. B. (1998). An internally consistent thermodynamic  
1021 data set for phases of petrological interest. *Journal of metamorphic Geology*, 16(3), 309-  
1022 343.

1023 Holland, TJB, Baker, JM & Powell, R (1998) Mixing properties and activity-composition  
1024 relationships of chlorites in the system MgO-FeO-Al<sub>2</sub>O<sub>3</sub>-SiO<sub>2</sub>-H<sub>2</sub>O. *European Journal of*  
1025 *Mineralogy*, 10, 395-406.

1026 Inui, M. (2006). Forward calculation of zoned garnet growth with limited diffusion  
1027 transport in the matrix. *Mineralogy and Petrology*, 88(1-2), 29-46.

1028 Jackson, M.G., Cabral, A.R., Rose-Koga, E.F., Koga, K., Price, A., Hauri, E.H., and Michael, P.  
1029 (2015). Ultra-depleted melts in olivine-hosted melt inclusions from the Ontong Java  
1030 Plateau. *Chemical Geology* 414, 124-137.

1031 Jamtveit, B., Wogelius, R. A., and Fraser, D. G. (1993). Zonation patterns of skarn garnets:  
1032 Records of hydrothermal system evolution. *Geology*, 21(2), 113-116.

1033 Jamtveit, B., and Hervig, R. L. (1994). Constraints on transport and kinetics in  
1034 hydrothermal systems from zoned garnet crystals. *Science*, 263(5146), 505-508.

1035 Jochum, K. P., Weis, U., Stoll, B., Kuzmin, D., Yang, Q., Raczek, I., ... and Enzweiler, J.  
1036 (2011). Determination of reference values for NIST SRM 610–617 glasses following ISO  
1037 guidelines. *Geostandards and Geoanalytical Research*, 35(4), 397-429.

1038 Joyce, J. (1991). Blueschist metamorphism and deformation on the Samana Peninsula; a  
1039 record of subduction and collision in the Greater Antilles. *Geologic and tectonic*  
1040 *development of the North America-Caribbean plate boundary in Hispaniola. Geological*  
1041 *Society of America Special Paper*, 262, 47-76.

1042 Keller, L.M., De Capitani, C. and Abart, R., 2005. A quaternary solution model for white  
1043 micas based on natural coexisting phengite–paragonite pairs. *Journal of*  
1044 *Petrology*, 46(10), pp.2129-2144.

1045 Kessel, R., Schmidt, M. W., Ulmer, P., and Pettke, T. (2005). Trace element signature of  
1046 subduction-zone fluids, melts and supercritical liquids at 120–180 km  
1047 depth. *Nature*, 437(7059), 724-727.

1048 Kohn, M. J. (2004). Oscillatory-and sector-zoned garnets record cyclic (?) rapid thrusting  
1049 in central Nepal. *Geochemistry, Geophysics, Geosystems*, 5(12).

1050 Konrad-Schmolke, M., Handy, M.R., Babist, J. and O'Brien, P.J. (2005). Thermodynamic  
 1051 modelling of diffusion-controlled garnet growth. *Contributions to Mineralogy and*  
 1052 *Petrology* 149(2): 181-195.

1053 Konrad-Schmolke, M., O'Brien, P. J., de Capitani, C., and Carswell, D. A. (2008a). Garnet  
 1054 growth at high-and ultra-high pressure conditions and the effect of element  
 1055 fractionation on mineral modes and composition. *Lithos*, 103(3-4), 309-332.

1056 Konrad-Schmolke, M., Zack, T., O'Brien, P. J., and Jacob, D. E. (2008b). Combined  
 1057 thermodynamic and rare earth element modelling of garnet growth during subduction:  
 1058 examples from ultrahigh-pressure eclogite of the Western Gneiss Region, Norway. *Earth*  
 1059 *and Planetary Science Letters*, 272(1-2), 488-498.

1060 Konrad-Schmolke, M., Zack, T., O'Brien, P. J., and Barth, M. (2011). Fluid migration above  
 1061 a subducted slab—Thermodynamic and trace element modelling of fluid–rock  
 1062 interaction in partially overprinted eclogite-facies rocks (Sesia Zone, Western  
 1063 Alps). *Earth and Planetary Science Letters*, 311(3-4), 287-298.

1064 Konrad-Schmolke, M., Halama, R., Wirth, R., Thomen, A., Klitscher, N., Morales, L., ... and  
 1065 Wilke, F. D. (2018). Mineral dissolution and reprecipitation mediated by an amorphous  
 1066 phase. *Nature communications*, 9(1), 1-9.

1067 Kotková, J. and Harley, S.L. (2010). Anatexis during High-pressure Crustal  
 1068 Metamorphism: Evidence from Garnet-Whole-rock REE Relationships and Zircon-Rutile  
 1069 Ti-Zr Thermometry in Leucogranulites from the Bohemian Massif. *Journal of Petrology*,  
 1070 51 (10): 1967-2001.

1071 Kulhánek, J., Faryad, S.W., Jedlička, R. and Svojtka, M., (2021). Dissolution and  
 1072 reprecipitation of garnet during eclogite facies metamorphism; major and trace elements  
 1073 budget for new garnet formation. *Journal of Metamorphic Geology (in press)*.

1074 Kumamoto, K.M, Warren, J.M., and Hauri, E.H. (2017) New SIMS reference materials for  
 1075 measuring water in upper mantle minerals. *American Mineralogist* 102, 537-547.

1076 Lanari, P., Vidal, O., De Andrade, V., Dubacq, B., Lewin, E., Grosch, E. G., and Schwartz, S.  
 1077 (2014). XMapTools: A MATLAB©-based program for electron microprobe X-ray image  
 1078 processing and geothermobarometry. *Computers and Geosciences*, 62, 227-240.



1079 Lasaga, A.C., and Jiang, J.X. (1995). Thermal History of Rocks - P-T-t Paths from  
 1080 Geospeedometry, Petrological Data, and Inverse-Theory Techniques. *American Journal of*  
 1081 *Science* 295(6): 697-741.

1082 Lesne, P., Kohn, S.C., Blundy, J., Witham, F., Botcharnikov, R.E., and Behrens, H. (2011)  
 1083 Experimental simulation of closed-system degassing in the system basalt-H<sub>2</sub>O-CO<sub>2</sub>-S-Cl.  
 1084 *Journal of Petrology*, 52 (9), 1737-1762.

1085 Loewe, K., Benke, D., Kübel, C., Lienig, T., Skokov, K. P., and Gutfleisch, O. (2017). Grain  
 1086 boundary diffusion of different rare earth elements in Nd-Fe-B sintered magnets by  
 1087 experiment and FEM simulation. *Acta Materialia*, 124, 421-429.

1088 Mann, P., Draper, G., and Lewis, J. F. (1991). An overview of the geologic and tectonic  
 1089 development of Hispaniola. *Geologic and tectonic development of the North America-*  
 1090 *Caribbean plate boundary in Hispaniola. Geological Society of America Special Paper*, 262,  
 1091 1-28.

1092 Manning, C. F., and Bohlen, S. R. (1991). The reaction titanite+ kyanite= anorthite+ rutile  
 1093 and titanite-rutile barometry in eclogites. *Contributions to Mineralogy and*  
 1094 *Petrology*, 109(1), 1-9.

1095 Marti, S., Füsseis, F., Butler, I. B., Schlepütz, C., Marone, F., Gilgannon, J., ... and Yang, Y.  
 1096 (2021). Time-resolved grain-scale 3D imaging of hydrofracturing in halite layers  
 1097 induced by gypsum dehydration and pore fluid pressure buildup. *Earth and Planetary*  
 1098 *Science Letters*, 554, 116679.

1099 McCammon, C and Kopylova, M.G. (2004). A redox profile of the Slave mantle and  
 1100 oxygen fugacity control in the cratonic mantle. *Contrib Mineral. Petrol.*, 148: 55-68.

1101 Meinhold, G., 2010. Rutile and its applications in earth sciences. *Earth-Science*  
 1102 *Reviews*, 102(1-2), pp.1-28.

1103 Meth, C.E. and Carlson, W.D. (2005). Diffusion-controlled synkinematic growth of garnet  
 1104 from a heterogeneous precursor at Passo del Sole, Switzerland. *The Canadian*  
 1105 *Mineralogist*, 43, 157-182.

1106 Moore, S. J., Carlson, W. D., and Hesse, M. A. (2013). Origins of yttrium and rare earth  
 1107 element distributions in metamorphic garnet. *Journal of Metamorphic Geology*, 31(6),  
 1108 663-689.

- 1109 Moyen, J. F. (2009). High Sr/Y and La/Yb ratios: the meaning of the “adakitic  
1110 signature”. *Lithos*, 112(3-4), 556-574.
- 1111 Moynihan, D.P. and Pattison, D.R.M., 2013. An automated method for the calculation of  
1112 P–T paths from garnet zoning, with application to metapelitic schist from the Kootenay  
1113 Arc, British Columbia, Canada. *Journal of Metamorphic Geology*, 31(5), pp.525-548.
- 1114 Mulrooney, D., and Rivers, T. (2005). Redistribution of the rare-earth elements among  
1115 coexisting minerals in metamafic rocks across the epidote-out isograd: an example from  
1116 the St. Anthony Complex, Northern Newfoundland, Canada. *The Canadian  
1117 Mineralogist*, 43(1), 263-294.
- 1118 Nagle, F. (1974). Blueschist, eclogite, paired metamorphic belts, and the early tectonic  
1119 history of Hispaniola. *Geological Society of America Bulletin*, 85(9), 1461-1466.
- 1120 O’Brien, P. J., 1997, Garnet zoning and reaction textures in overprinted eclogites,  
1121 Bohemian Massif, European Variscides; a record of their thermal history during  
1122 exhumation: *Lithos*, v. 41, p. 119-133.
- 1123 Oliver, N. H., and Bons, P. D. (2001). Mechanisms of fluid flow and fluid–rock interaction  
1124 in fossil metamorphic hydrothermal systems inferred from vein–wallrock patterns,  
1125 geometry and microstructure. *Geofluids*, 1(2), 137-162.
- 1126 Otamendi, J. E., de La Rosa, J. D., Douce, A. E. P., and Castro, A. (2002). Rayleigh  
1127 fractionation of heavy rare earths and yttrium during metamorphic garnet  
1128 growth. *Geology*, 30(2), 159-162.
- 1129 Paton, C., Hellstrom, J., Paul, B., Woodhead, J., and Hergt, J. (2011). Iolite: Freeware for  
1130 the visualisation and processing of mass spectrometric data. *Journal of Analytical Atomic  
1131 Spectrometry*, 26(12), 2508-2518.
- 1132 Pollington, A. D., and Baxter, E. F. (2011). High precision microsampling and preparation  
1133 of zoned garnet porphyroblasts for Sm–Nd geochronology. *Chemical Geology*, 281(3-4),  
1134 270-282.
- 1135 Pyle, J. M., and Spear, F. S. (1999). Yttrium zoning in garnet: coupling of major and  
1136 accessory phases during metamorphic reactions. *Geological Materials Research*, 1(6), 1-  
1137 49.
- 1138 Ranjbar, S., Manesh, S. T., Mackizadeh, M. A., Tabatabaei, S. H., and Parfenova, O. V.  
1139 (2016). Geochemistry of major and rare earth elements in garnet of the Kal-e Kafi skarn,

1140 Anarak Area, Central Iran: Constraints on processes in a hydrothermal  
 1141 system. *Geochemistry International*, 54(5), 423-438.

1142 Reynes, J., Jollands, M., Hermann, J., and Ireland, T. (2018). Experimental constraints on  
 1143 hydrogen diffusion in garnet. *Contributions to Mineralogy and Petrology* 173:69

1144 Reynes, J., Lanari, P., and Hermann, J. (2020). A mapping approach for the investigation  
 1145 of Ti–OH relationships in metamorphic garnet. *Contributions to Mineralogy and*  
 1146 *Petrology*, 175, 1-17.

1147 Rubatto, D. (2002). Zircon trace element geochemistry: partitioning with garnet and the  
 1148 link between U–Pb ages and metamorphism. *Chemical geology*, 184(1-2), 123-138.

1149 Rubatto, D., Burger, M., Lanari, P., Hattendorf, B., Schwarz, G., Neff, C., ... and Günther, D.  
 1150 (2020). Identification of growth mechanisms in metamorphic garnet by high-resolution  
 1151 trace element mapping with LA-ICP-TOFMS. *Contributions to Mineralogy and*  
 1152 *Petrology*, 175(61), 61.

1153 Sassi, R., Harte, B., Carswell, D. A. and Yujing, H., 2000, Trace element distribution in  
 1154 Central Dabie eclogites: *Contributions to Mineralogy and Petrology*, v. 139, p. 298-315.

1155 Scibiorski, E., Kirkland, C. L., Kemp, A. I. S., Tohver, E., & Evans, N. J. (2019). Trace  
 1156 elements in titanite: A potential tool to constrain polygenetic growth processes and  
 1157 timing. *Chemical Geology*, 509, 1-19.

1158 Shrestha, S., Larson, K. P., Duesterhoeft, E., Soret, M., and Cottle, J. M. (2019).  
 1159 Thermodynamic modelling of phosphate minerals and its implications for the  
 1160 development of PTt histories: A case study in garnet-monazite bearing  
 1161 metapelites. *Lithos*, 334, 141-160.

1162 Sibson, R.H., 1994. Crustal stress, faulting and fluid flow. *Geological Society, London,*  
 1163 *Special Publications*, 78(1), pp.69-84.

1164 Skora, S., Baumgartner, L. P., Mahlen, N. J., Johnson, C. M., Pilet, S., and Hellebrand, E.  
 1165 (2006). Diffusion-limited REE uptake by eclogite garnets and its consequences for Lu–Hf  
 1166 and Sm–Nd geochronology. *Contributions to Mineralogy and Petrology*, 152(6), 703-720.

1167 Spear, F.S. and Daniel, C.G. (2001). Diffusion control of garnet growth, Harpswell Neck,  
 1168 Maine, USA. *Journal of Metamorphic Geology* 19(2): 179-195.

1169 Spear, F.S. and Selverstone, J. (1983). Quantitative P-T path from zoned minerals; theory  
 1170 and tectonic applications. *Contributions to Mineralogy and Petrology*, 83(3-4): 348-357.

1171 Stowell, H., Zuluaga, C., Boyle, A., and Bulman, G. (2011). Garnet sector and oscillatory  
 1172 zoning linked with changes in crystal morphology during rapid growth, North Cascades,  
 1173 Washington. *American Mineralogist*, 96(8-9), 1354-1362.

1174 Taetz, S., John, T., Bröcker, M., Spandler, C., and Stracke, A. (2018). Fast intraslab fluid-  
 1175 flow events linked to pulses of high pore fluid pressure at the subducted plate  
 1176 interface. *Earth and Planetary Science Letters*, 482, 33-43.

1177 Tirone, M., Ganguly, J., Dohmen, R., Langenhorst, F., Hervig, R., and Becker, H. W. (2005).  
 1178 Rare earth diffusion kinetics in garnet: experimental studies and  
 1179 applications. *Geochimica et Cosmochimica Acta*, 69(9), 2385-2398.

1180 Ubide, T., McKenna, C. A., Chew, D. M., and Kamber, B. S. (2015). High-resolution LA-ICP-  
 1181 MS trace element mapping of igneous minerals: In search of magma histories. *Chemical*  
 1182 *Geology*, 409, 157-168.

1183 Usui, T., Kobayashi, K., Nakamura, E., and Helmstaedt, H. (2007). Trace element  
 1184 fractionation in deep subduction zones inferred from a lawsonite-eclogite xenolith from  
 1185 the Colorado Plateau. *Chemical Geology*, 239(3-4), 336-351.

1186 Van Orman, J. A., Grove, T. L., and Shimizu, N. (2001). Rare earth element diffusion in  
 1187 diopside: influence of temperature, pressure, and ionic radius, and an elastic model for  
 1188 diffusion in silicates. *Contributions to Mineralogy and Petrology*, 141(6), 687-703.

1189 Viete, D. R., Hacker, B. R., Allen, M. B., Seward, G. G., Tobin, M. J., Kelley, C. S., ... and  
 1190 Duckworth, A. R. (2018). Metamorphic records of multiple seismic cycles during  
 1191 subduction. *Science advances*, 4(3), eaaq0234.

1192 Wei, C.J., Powell, R. and Zhang, L.F., 2003. Eclogites from the south Tianshan, NW China:  
 1193 petrological characteristic and calculated mineral equilibria in the Na<sub>2</sub>O–CaO–FeO–  
 1194 MgO–Al<sub>2</sub>O<sub>3</sub>–SiO<sub>2</sub>–H<sub>2</sub>O system. *Journal of Metamorphic Geology*, 21(2), pp.163-179.

1195 White, R.W., Powell, R. and Phillips, G.N., 2003. A mineral equilibria study of the  
 1196 hydrothermal alteration in mafic greenschist facies rocks at Kalgoorlie, Western  
 1197 Australia. *Journal of Metamorphic Geology*, 21(5), pp.455-468.

1198 White, RW, Powell, R & Holland, TJB (2007) Progress relating to calculation of partial  
 1199 melting equilibria for metapelites. *Journal of Metamorphic Geology*, 25, 511-527.

Whitehouse, M. J. and Platt, J. P., 2003, Dating high grade metamorphism - constraints from rare-earth elements in zircon and garnet: Contributions to Mineralogy and Petrology, v. 145, p. 61-74.

Yang, P. and Rivers, T. (2002). The origin of Mn and Y annuli in garnet and the thermal dependence of P in garnet and Y in apatite in calc-pelite and pelite, Gagnon terrane, western Labrador. Geological Materials Research, 4 (1).

Zhai, D. G., Liu, J. J., Zhang, H. Y., Wang, J. P., Su, L., Yang, X. A., and Wu, S. H. (2014). Origin of oscillatory zoned garnets from the Xieertala Fe–Zn skarn deposit, northern China: In situ LA–ICP–MS evidence. *Lithos*, 190, 279-291.

### Figure captions

**Fig.1:** Petrography of the investigated sample. a) Thin section photomicrograph of the sample showing several large euhedral garnet grains within a matrix of sodic amphibole (Nam), quartz (Qtz), white mica (WM), chlorite (Chl), titanite (Ttn) and apatite (Ap). The investigated garnet (upper right corner) has a darker core with numerous titanite inclusions (not visible) and a brighter rim with large rutile (Rt) inclusions. The horizontal line within the grain are laser ablation pits. b) Crossed polarizers photomicrograph of a sodic amphibole with inclusions of relict omphacite (whitish interference colours). c) Back scattered electron detail image of relict omphacite inclusions in sodic amphibole. The omphacite inclusions indicate the samples eclogite-facies metamorphic history, whereas the matrix minerals reflect the blueschist-facies retrograde equilibration.

**Fig. 2:** Details of the investigated garnet grain. a) Close up photomicrograph of the chosen garnet. Clearly visible are the darker core overgrown by a lighter rim. Visible inclusions in the core are quartz and apatite, in the rim numerous inclusions of brownish rutile are striking. The laser ablation pits in the vertical profile have diameters of 50µm. b) Major element microprobe maps from the area marked in (a) indicating smooth compositional major element variations within the garnet grain. The numerous titanite inclusions in the core are visible as white spots in the Ca mapping. c) Quantitative microprobe profile across the garnet grain parallel to the laser ablation spots visible in a). The major element zoning is typical for high pressure garnets with high almandine content the zoning of which mirrors that of the spessartine component.

Slightly decreasing grossular and increasing pyrope components reflect the samples prograde metamorphic evolution.

**Fig. 3:** Rare earth element variations in the investigated garnet grain. a) HREE+Y maps of the area indicated in Fig. 2a. The HREE+Y maps show a complex compositional pattern with an area of high concentrations in the core, a broad enrichment zone at the core-rim transition and six smaller concentric peaks with associated troughs (see Tm map) more or less evenly distributed throughout the entire grain outside the inner core. The transition from titanite (ttn) and rutile (rt) inclusions is shown in the Lu and Ho maps and correlates well with the broad HREE+Y enrichment zone. b) Core-rim HREE+Y profiles extracted from the maps in a). All HREE+Y show a broad pattern with decreasing concentrations from the centre of the core to about 30% radius followed by an increase peaking at 70% radius and a significant decrease towards the rim. Superimposed on this broad pattern are six evenly distributed minor peaks that appear in all HREE+Y profiles at the same position. Thin black lines are the measured data, bold red lines are low-pass frequency filtered data.

**Fig.4:** HREE distribution patterns of peaks and troughs extracted from the maps in Fig. 1. From peaks to the associated troughs the convex upward curvature of the HREE distribution patterns is increasing due to preferential fractionation of the heaviest REE, whereas from troughs to the next peak the pattern curvature does not change significantly as all HREE are evenly replenished. See text for further explanation.

**Fig.5:** Correlation of (RGB)  $\mu$ -Raman map with the thin section photomicrograph. The  $\mu$ -Raman map shows that titanite (ttn) inclusions (yellow) are found in the core, whereas rutile (rt) inclusions (red) are restricted to the rim of the garnet grain. Within a narrow zone both Ti phases coexist. Titanite inclusions in the rim are always associated with cracks and are related to the exhumation of the sample as do the titanites in the matrix. Apatite inclusions (orange) can be found throughout the entire crystal. WM = white mica.

**Fig. 6:** Results of the SIMS measurements of water, fluid mobile elements (FMEs), magnesium and titanium. The positions of the measured spots are along a core-to-inner rim profile and are shown in the Tm map in the upper right panel. The position within the large Tm map is shown in Fig. 3. The grey bars in the diagrams indicate the approximate positions of the REE peaks shown in Fig. 3. Neither the concentrations of the FMEs, nor those of water, MgO and TiO<sub>2</sub> are fluctuating such as the REEs indicated by the lack of correlation with the peak positions. The arrows in the TiO<sub>2</sub> diagram mark spots with a potential contribution of titanite inclusions.

**Fig. 7:** Summary of the thermodynamic forward modelling results. a) Calculated *P-T* pseudosection for the bulk rock composition of our sample (Table 1). The black arrow marks the *P-T* trajectory along which the rock evolution and garnet growth was modelled. The path follows the results of Escuder-Viruete and Pérez-Estaún 2006 (E+P 06). The grey circles show the proposed garnet growth stages from E+P 06. The grey rectangles mark the peak *P-T* conditions for the Punta Balandra rocks from E+P 06. The grey arrow shows the proposed retrograde *P-T* trajectory and the hatched area marks the *P-T* region of the matrix assemblage equilibration in our sample. b) Normalized mineral assemblage coexisting with garnet along the modelled *P-T* trajectory. Garnet grows from the decomposition of chlorite and epidote. The titanite-out reaction is superimposed with an Avrami-type reaction progress. New garnet and white mica plot on the right axis. c) The modelled garnet composition reflects well the observed growth zonation in the natural sample.

**Fig. 8:** Modelled REE growth zonations expected for garnet growth along the *P-T* trajectory shown in Fig. 6a. The bold lines represent the REE growth zonations without the titanite-out reaction, the connected circles show the effect of titanite breakdown on the REE profiles. Additionally shown in the Lu diagram are the expected growth zonation assuming Rayleigh fraction (bold stippled line) as well as lines indicating different peak widths as a result of garnet equilibration with different fractions of the matrix minerals (thin solid lines). The numbers indicate the fractions of matrix minerals the garnet is in equilibrium with. See text for further explanations.

1294

1295 **Fig. 9:** REE compositional correlation of host garnet and titanite inclusions. a) Eu/Yb  
1296 ratios in titanite inclusions extracted from the REE mapping. Eu/Yb in the inclusions is  
1297 increasing from garnet centre to a crest marked by the dash dotted line. Beyond that  
1298 crest the Eu/Yb ratios are decreasing until the titanite-out reaction zone. b) Eu/Yb ratio  
1299 in garnet parallels that in the titanite inclusions indicating a continuous equilibration of  
1300 matrix minerals with the growing garnet. c) REE distribution patterns in the titanite  
1301 inclusions. The slope of the REE patterns is decreasing from garnet core to the garnet  
1302 mantle followed by an increase towards the reaction zone. Titanites in the reaction zone  
1303 have also higher REE concentrations caused by the higher availability of REE during  
1304 titanite breakdown. d) Map of  $\frac{Eu}{Yb}$  values extracted from the trace element  
1305 mapping. The  $\frac{Eu}{Yb}$  values are relatively constant around 0.9 in the core  
1306 (yellow) and increase in the garnet rim to values of about 1.2 (red). Blue values  
1307 correspond to pixels with LREE values below detection limit. Notable is the absence of  
1308 fluctuations in the garnet core such as seen in the HREE mapping. See text for further  
1309 discussion.

1310 **Fig. 10:** Comparison of the results from a thermodynamic-geochemical garnet growth  
1311 model with the natural sample. a) Model results displaying the calculated Lu  
1312 concentration change assuming fractional equilibrium garnet crystallization (bold black  
1313 line) and diffusion-limited Lu uptake during seven garnet growth periods (thin black  
1314 line). The bold red line displays a possible Lu profile resulting from successive shifts  
1315 from diffusion-limited REE uptake to (fractional) equilibrium Lu incorporation. b)  
1316 Comparison of the modelled and observed Lu profile exhibits obvious similarities. The  
1317 bold black line reflects the fractional equilibrium Lu concentration, whereas the bold red  
1318 and thin black lines show the measured data which can be explained by a shift from  
1319 diffusion-limited to fractional equilibrium Lu uptake.

1320 **Fig. 11:** Conceptual model explanation. a) Garnet growth starts in equilibrium with a  
1321 rock volume that has a background permeability enabled by an interconnected and  
1322 potentially fluid-filled pore space in the ITM allowing for a certain continuous element  
1323 flux (left panel). REE incorporation into garnet follows fractional equilibrium  
1324 crystallization (middle panel). The REE concentration in garnet follows the bold black  
1325 line in the right panel. b) The permeability of the rock is decreasing, which leads to



closure of the pore space and to compartmentalization of the reacting rock volume (left panel). Garnet growth at this stage causes a rapid REE decrease in the compartmentalized ITM as well as at the garnet surface (middle panel), which leads to the development of the HREE troughs (right panel). c) Rock permeability increases (left panel) due to ongoing devolatilization reactions in the host rock. Increasing permeability re-establishes fluid percolation, which replenishes the REE budget available for the growing garnet (middle panel). REE concentration in garnet returns to the initial continuous background element flux (right panel). d) Recurrence of these steps together with the titanite-to-rutile transition leads to the development of the observed complex REE zonation patterns and REE distribution pattern in our sample.

**Table 1:** *Major element bulk rock composition used for the thermodynamic modelling.*

**Table 2:** *REE distribution coefficients for the geochemical modelling.*

**Table 3:** *Initial REE concentration of the sample as used for the thermodynamic-geochemical model.*

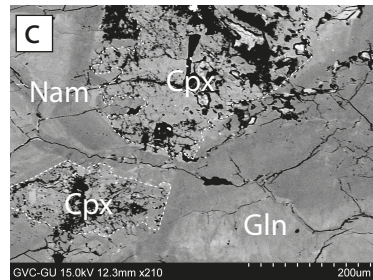
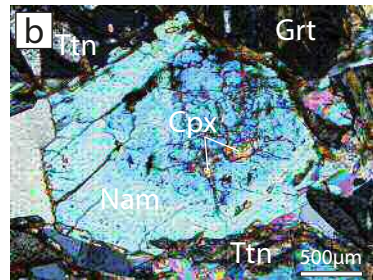
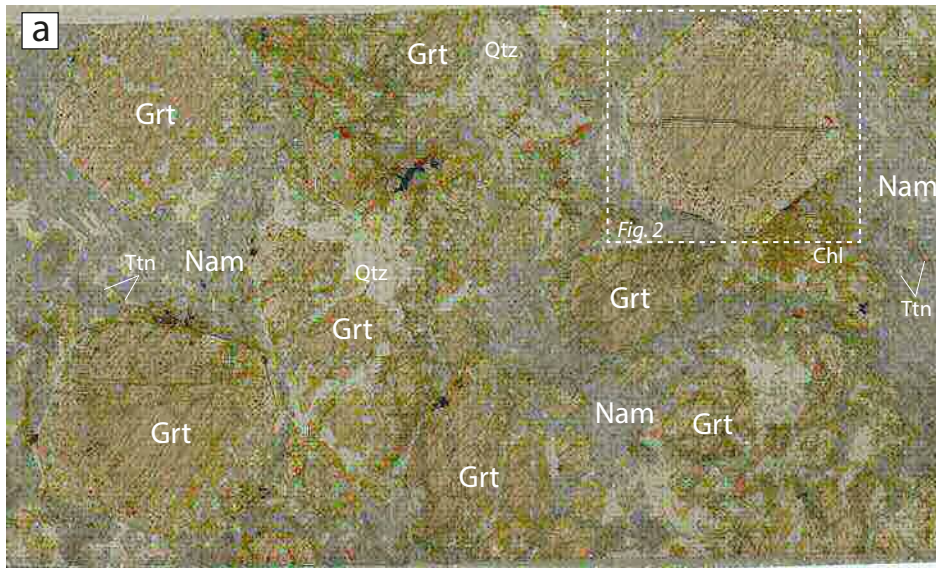


Figure 1

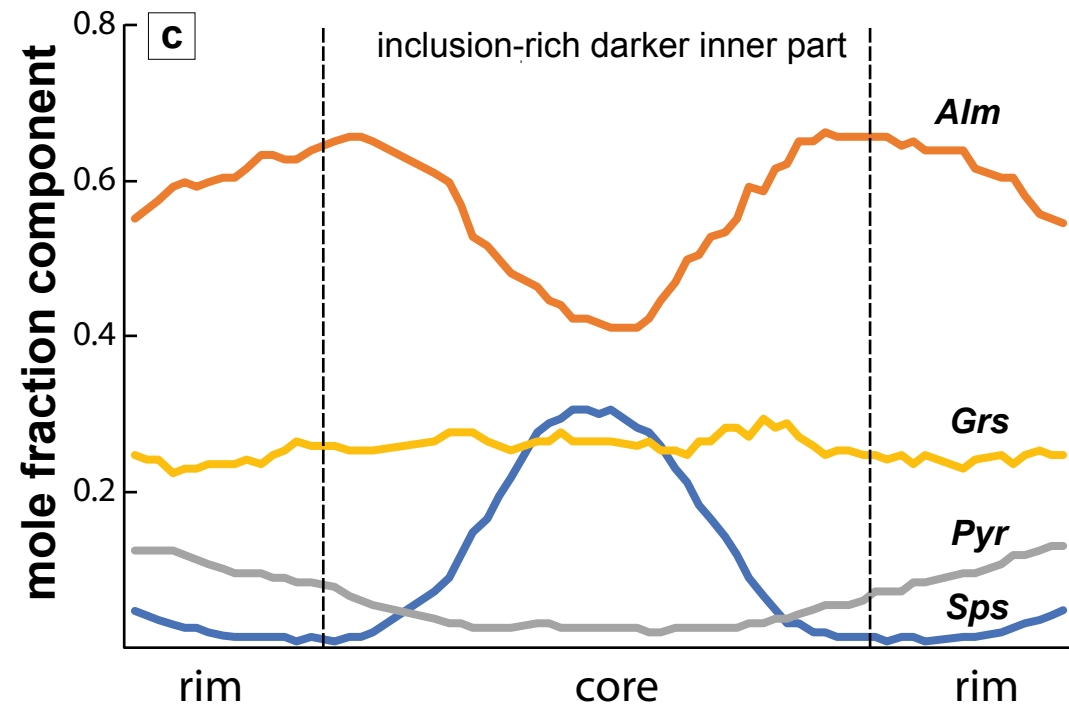
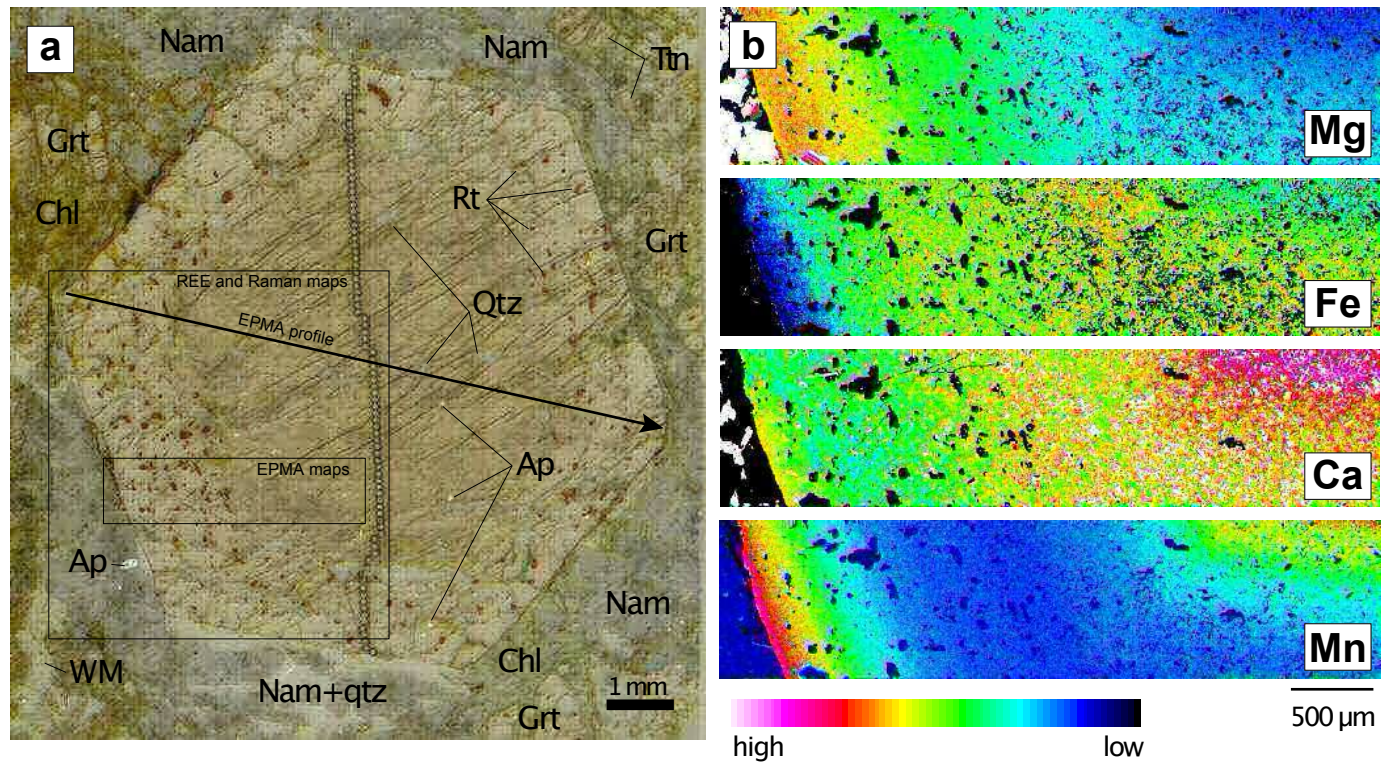


Figure 2



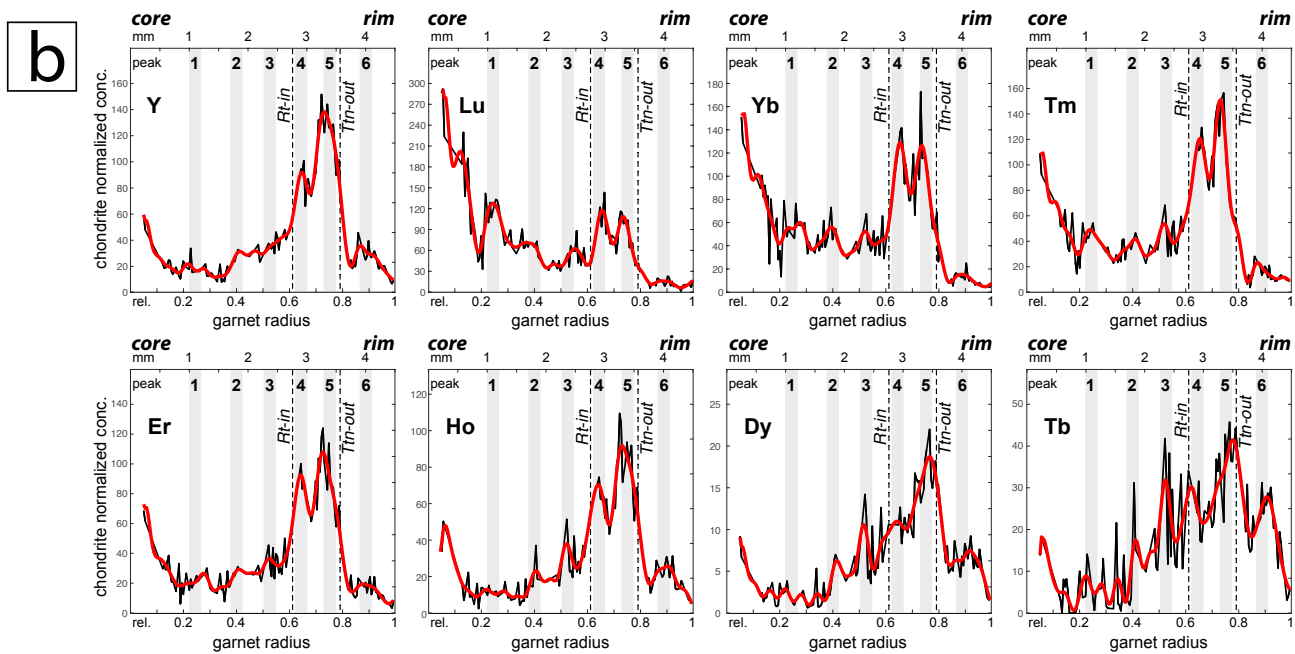
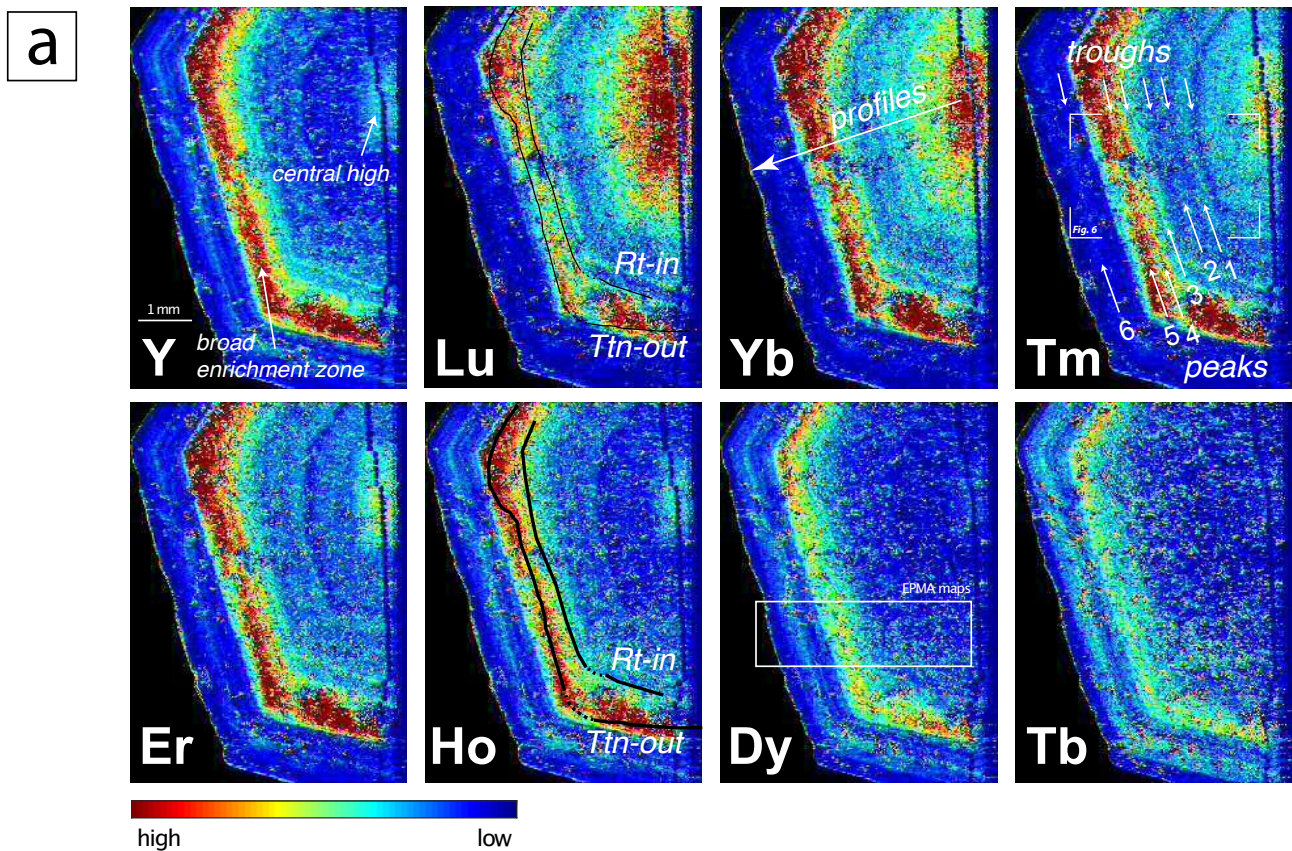


Figure 3

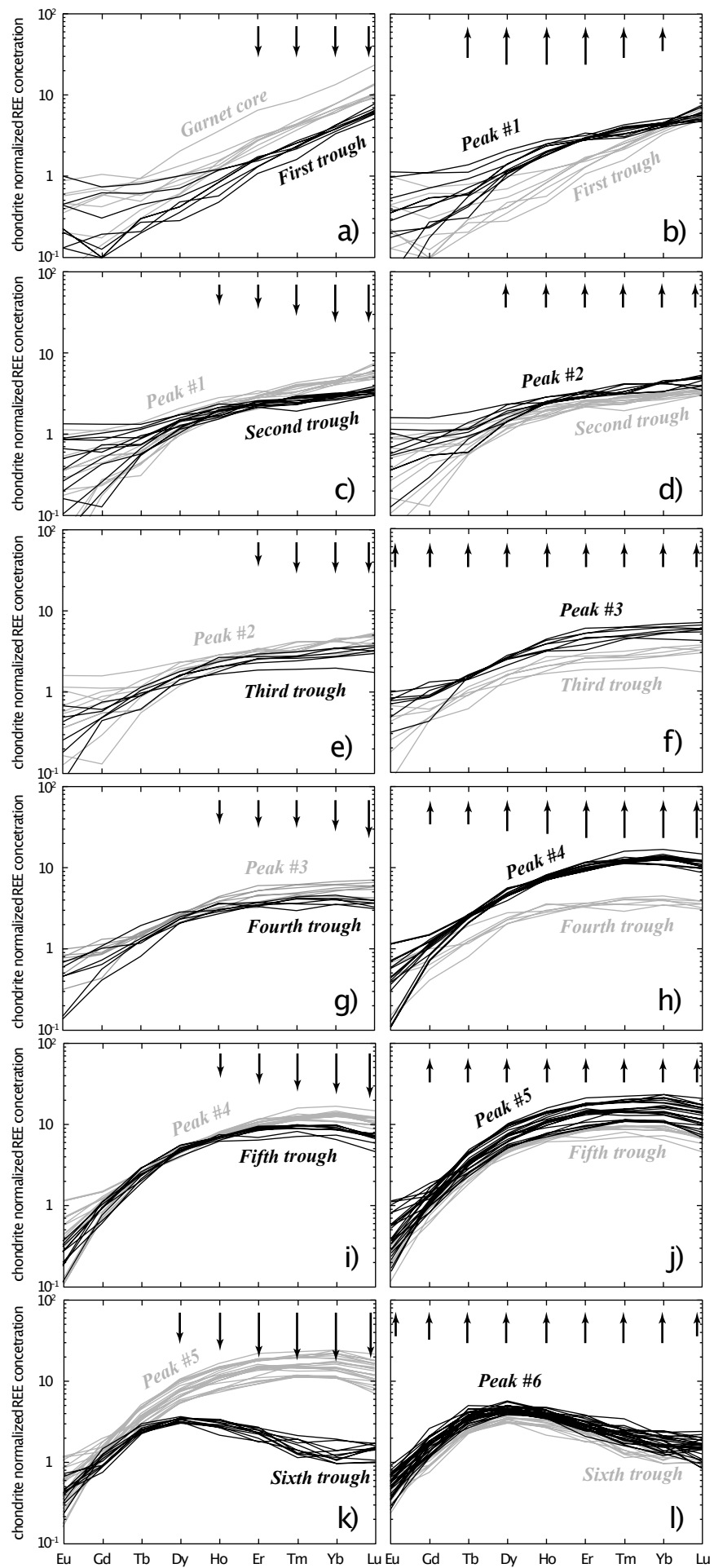


Figure 4



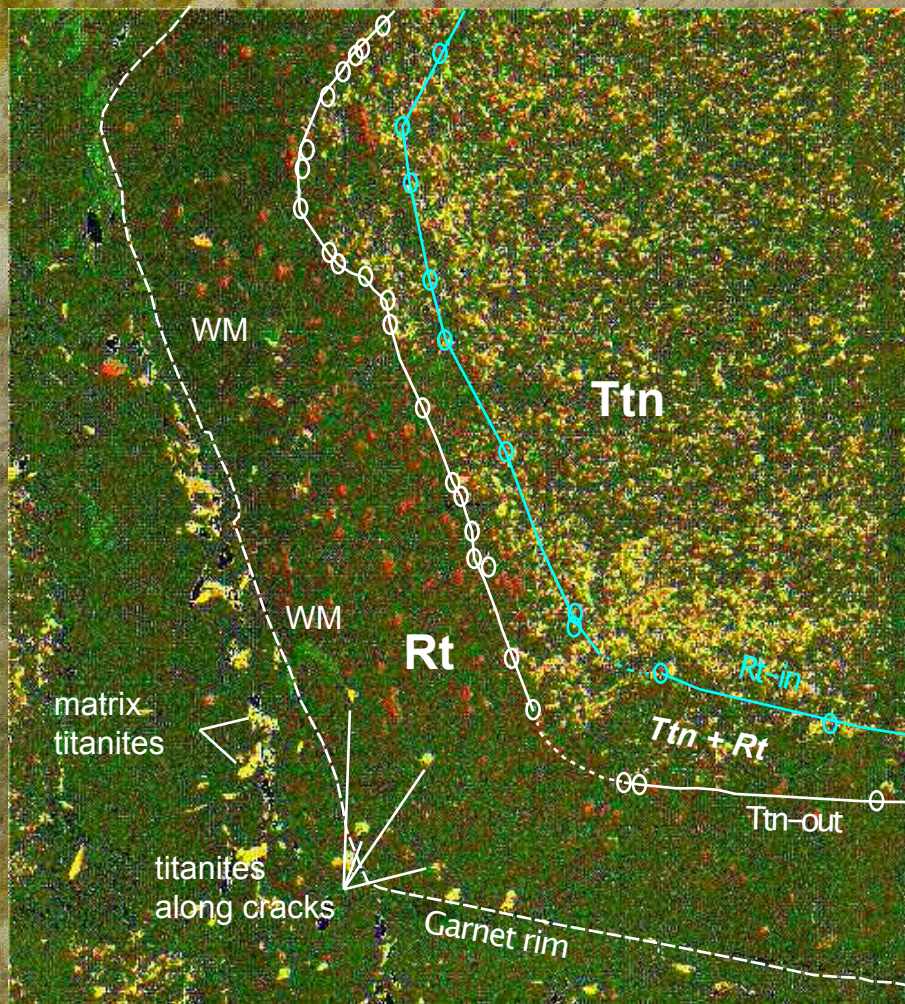


Figure 5

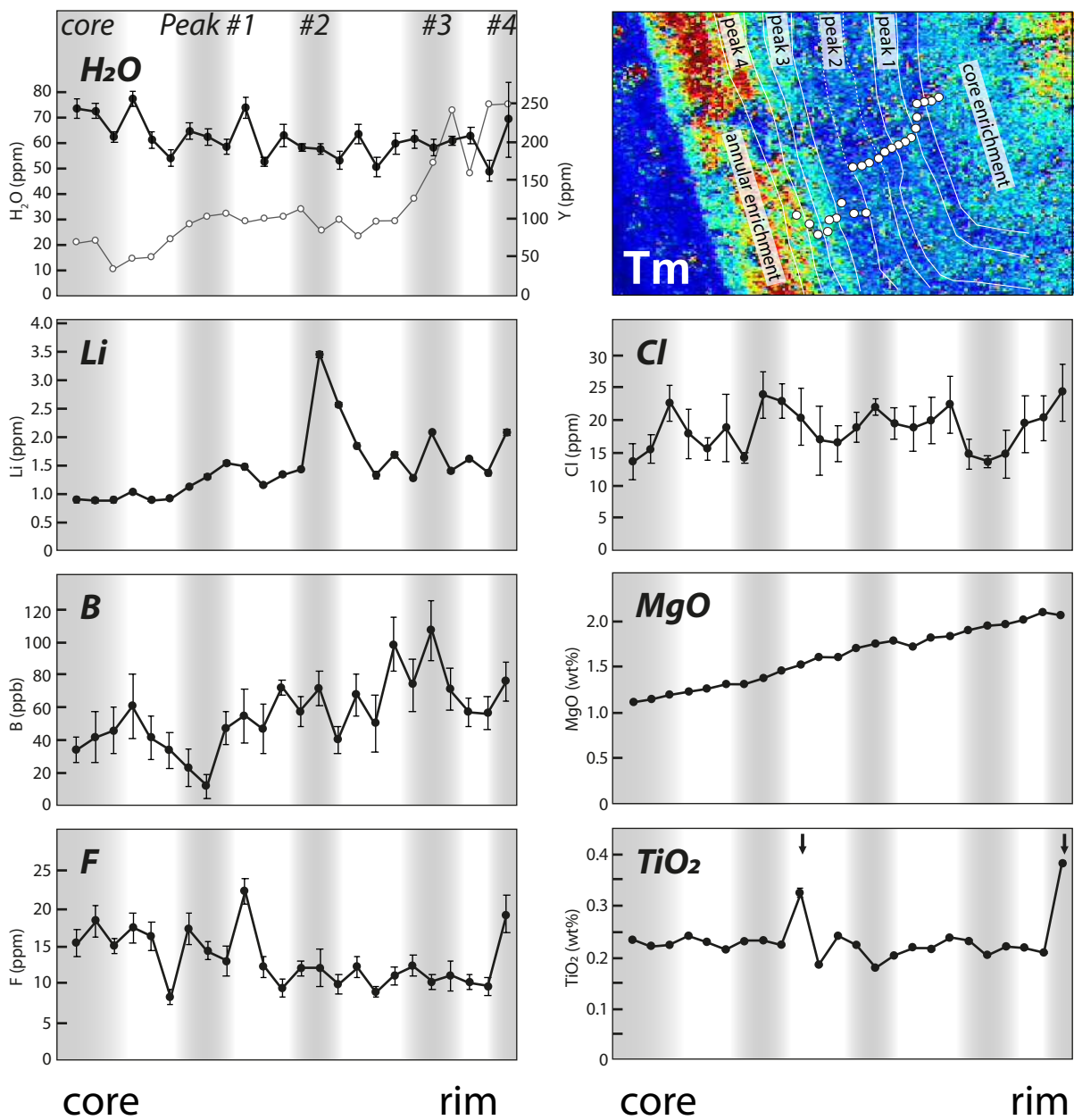


Figure 6



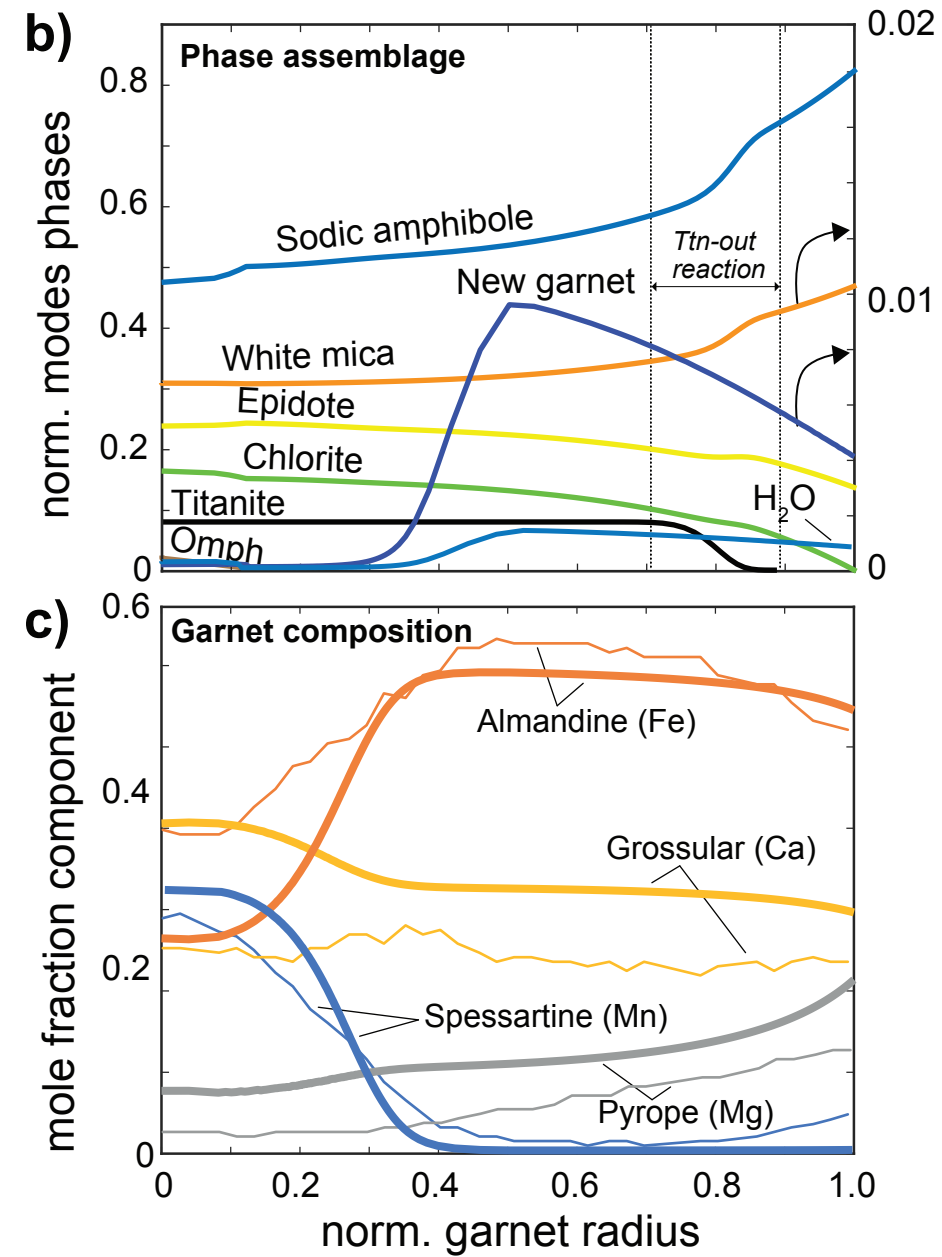
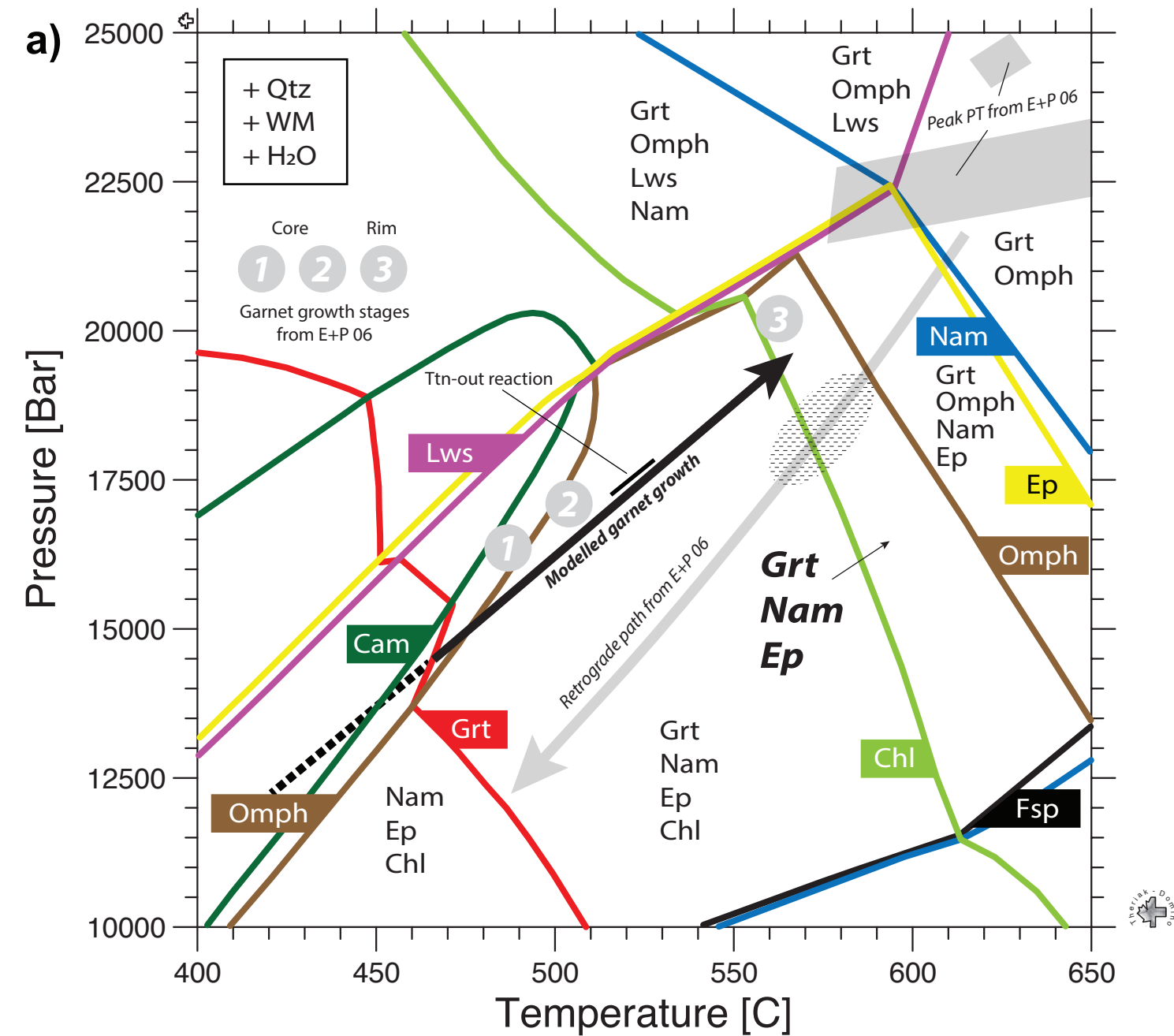


Figure 7



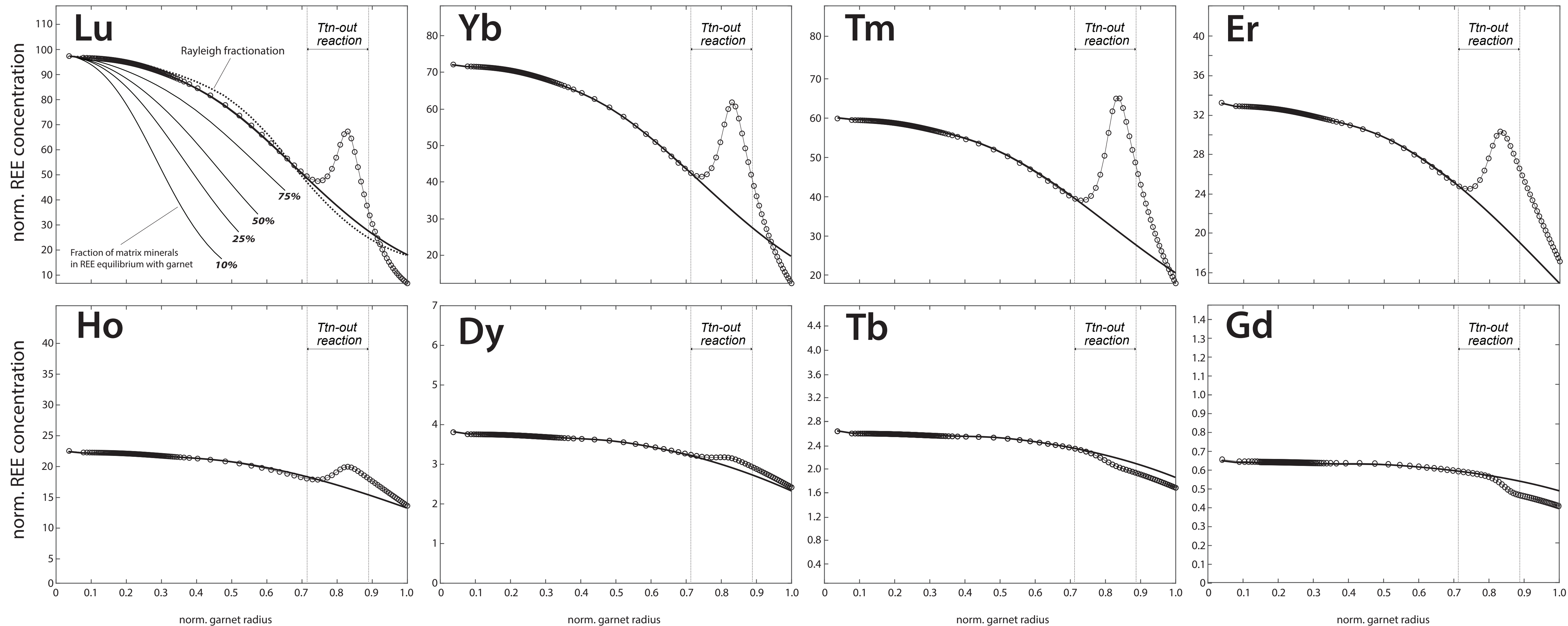


Figure 8

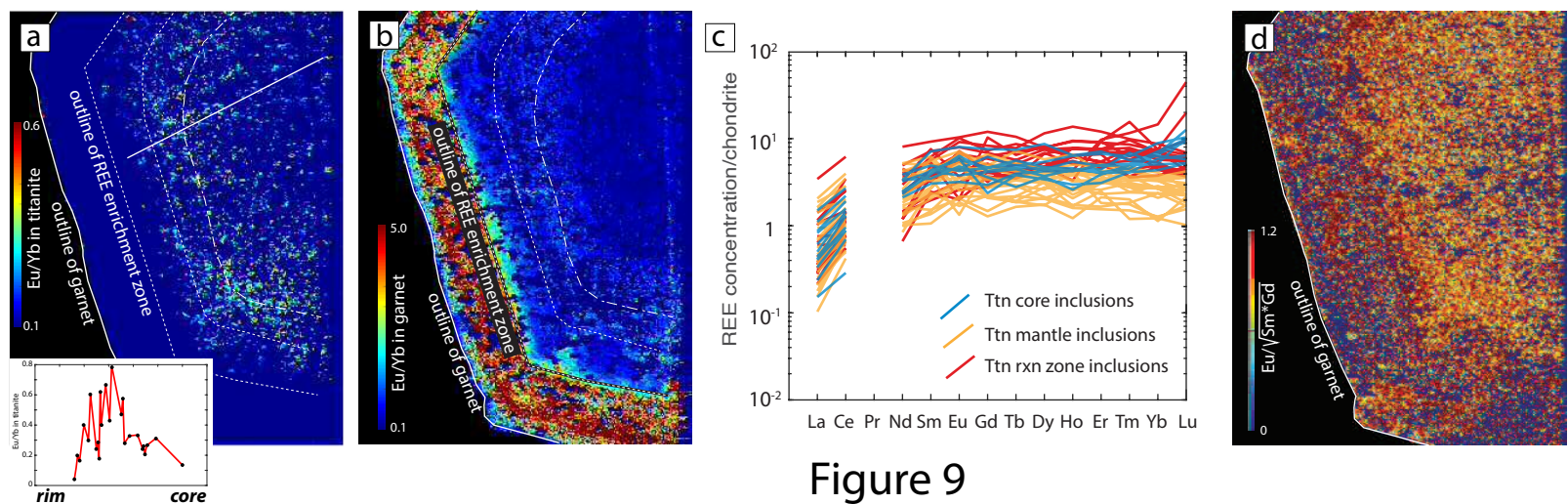


Figure 9

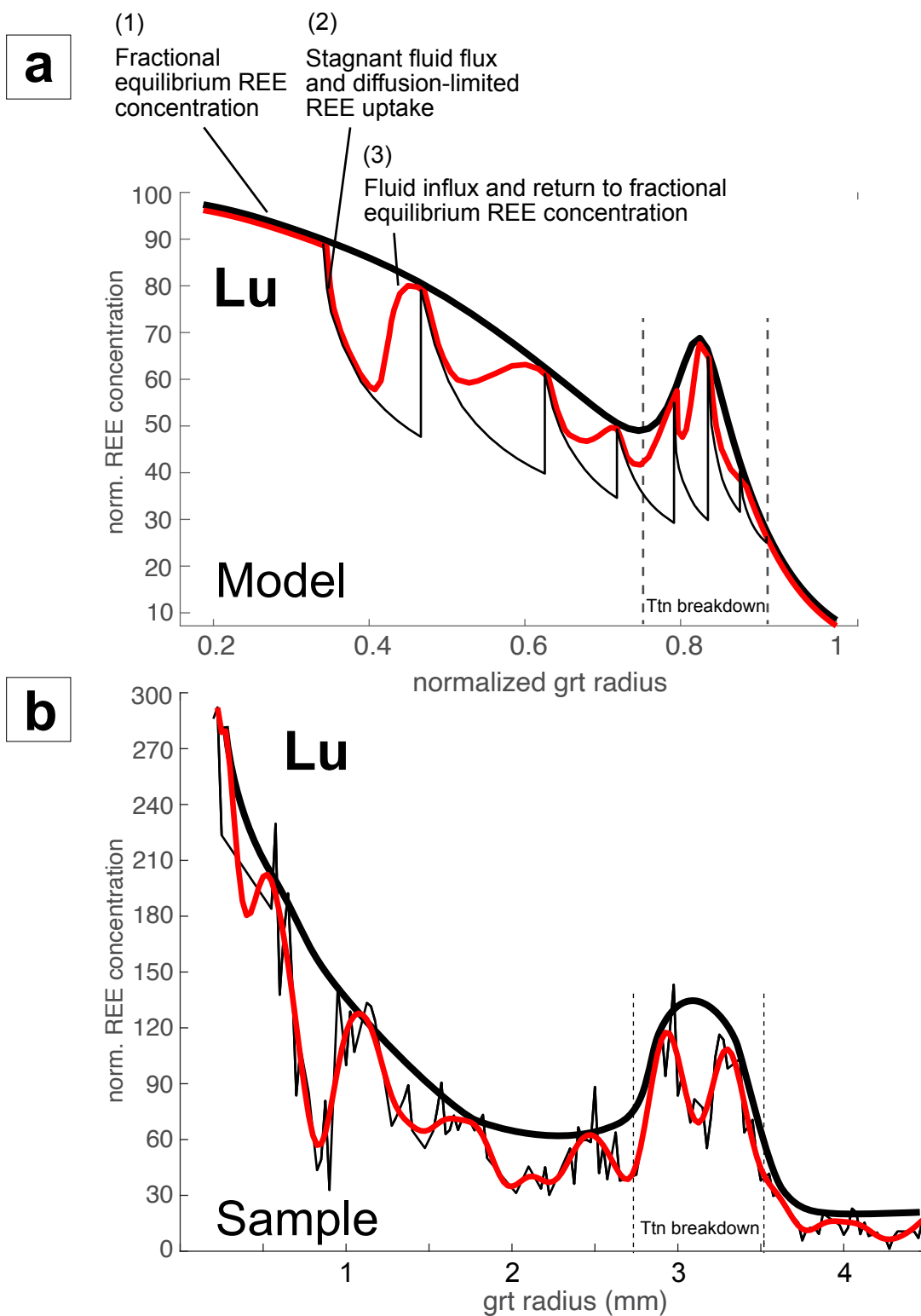


Figure 10



	Na	Ca	K	Fe	Mg	Al	Si	Mn	O	H
<b><i>Molar proportions</i></b>	4,402	8,172	0,095	7,775	13,471	14,51	47,574	0,05	IMR	Initially H <sub>2</sub> O saturated

	La	Ce	Pr	Nd	Sm	Eu	Gd	Tb	Dy	Ho	Er	Tm	Yb	Lu
<b><i>Amph/Grt<sup>1</sup></i></b>	4,62e4	3,528e4	1,46e4	4142	746	163	91,1	20,28	5,281	1,768	1,055	0,342	0,276	0,182
<b><i>Ep/Grt<sup>1</sup></i></b>	6,6e5	2,52e5	6,09e4	1,09e4	1022	223,5	70,152	12,08	2,614	0,731	0,348	0,097	0,071	0,042
<b><i>Cpx/Grt<sup>2</sup></i></b>	15	5,109	1,239	0,829	0,2	0,083	0,043	0,02	0,009	0,006	0,005	0,004	0,003	0,003
<b><i>Fluid/Grt<sup>3</sup></i></b>	0,728	0,432	0,2	0,051	0,012	0,009	0,005	0,004	0,004	0,003	0,003	0,002	0,002	0,002
<b><i>Chl/Grt<sup>4</sup></i></b>	1750	1328	450	191	23,3	4,440	1,771	0,25	0,054	0,02	0,01	0,008	0,002	0,002
<b><i>Ttn/Grt<sup>5</sup></i></b>	6805	2387	456,4	176,1	64,464	26,527	15,1	8,212	4,829	3,044	2,54	2,01	1,501	1,16

Sources: <sup>1</sup>Mulrooney and Rivers 2005; <sup>2</sup>Hermann 2002; <sup>3</sup>Kessel et al., 2005; <sup>4</sup>El Korh 2010; <sup>5</sup>Sassi et al., 2000

<i>Element</i>	<i>La</i>	<i>Ce</i>	<i>Pr</i>	<i>Nd</i>	<i>Sm</i>	<i>Eu</i>	<i>Gd</i>	<i>Tb</i>	<i>Dy</i>	<i>Ho</i>	<i>Er</i>	<i>Tm</i>	<i>Yb</i>	<i>Lu</i>
<i>initial bulk rock composition <math>\mu\text{g/g}</math></i>	5.8	16.4	2.8	14.5	4.4	1.5	6.5	1.0	6.6	1.5	4.2	0.7	3.9	0.6